land

MDPI

Article

Geomorphological Classification of Monogenetic Volcanoes and Its Implication to Tectonic Stress Orientation in the Middle Atlas Volcanic Field (Morocco)

Mohammed Benamrane [1,*], Károly Németh [2,3,4,5], Mohamed Jadid [1] and El Hassan Talbi [1]

[1] Geoheritage, Geoenvironment and Mining and Water Prospection Laboratory, Faculty of Science, Mohammed First University, Avenue Mohammed VI, B.P.717, Oujda 60050, Morocco
[2] School of Agriculture and Environment, Massey University, Palmerston North 4442, New Zealand
[3] Institute of Earth Physics and Space Science, Csatkai E. u. 6-8., 9400 Sopron, Hungary
[4] Saudi Geological Survey, Building No. 7885, Additional No. 3028, Jeddah 23352, Saudi Arabia
[5] Instituto Nazionale di Geofisica e Vulcanologia, Sezione di Bologna, Via Donato Creti 12, 40128 Bologna, Italy
* Correspondence: med.benamrane@ump.ac.ma; Tel.: +212-762-985-389

Abstract: The Middle Atlas Volcanic Field (MAVF) covers an area of 1500 km^2, with a total erupted volume of solid products (e.g., Dense Rock Equivalent or DRE) estimated to be more than 80 km^3. The MAVF comprises 87 monogenetic basaltic volcanoes of Tertiary-Quaternary age as scoria cones (71%) and maars (29%). These monogenetic basaltic volcanoes have various morphology (e.g., circular, semi-elliptic, elliptic in map views). They can be isolated or form clustered monogenetic complexes. They are largely grouped in the Middle Atlas, in an intraplate geotectonic context forming two distinct major alignments (N160–170° and N40–50°), each closely associated with regional structural elements. By the best estimates, the preserved bulk pyroclastic products do not exceed 0.7 km^3, and they show large textural and componentry diversity (e.g., bedded/unbedded, coarse/fine, dense/scoriaceous fallout and pyroclastic density current deposit, etc.). Lava flows also demonstrate great variety of preserved surface textures, including pāhoehoe, ʻaʻā, and clastogenic types. Morphostructural features of lava flows linked to lava flow dynamics have also been recognized, and the presence of hornitos, columnar jointed basaltic flow units, lava tubes, tumuli, and clastogenic lava flows have been recognized and mapped. Some half-sectioned dykes expose interior parts of magmatic shallow feeding pipes. The current morphology of the volcanoes of the MAVF reflects various syn- and post-eruptive processes, including (1) erosional features due to weathering, (2) gravitational instability during and after volcanic activity, (3) vegetation impact, and (4) successive burial of lava flows. The documented volcanic features of this typical monogenetic volcanic field form the core of the region's geoheritage elements and are considered to be unique in the new African geoheritage context. Hence, they will likely form the basis of future geotourism, geoeducation, and geoconservation ventures.

Keywords: Maar; scoria cone; lava flow; monogenetic volcanic field; Tertiary-Quaternary; intraplate; Middle Atlas

Citation: Benamrane, M.; Németh, K.; Jadid, M.; Talbi, E.H. Geomorphological Classification of Monogenetic Volcanoes and Its Implication to Tectonic Stress Orientation in the Middle Atlas Volcanic Field (Morocco). *Land* **2022**, *11*, 1893. https://doi.org/10.3390/land11111893

Academic Editors: Margaret Brocx and Vic Semeniuk

Received: 2 October 2022
Accepted: 23 October 2022
Published: 25 October 2022

1. Introduction

Monogenetic volcanism produces small-volume volcanoes (≤1 km^3), which have been erupted through one continuous or many discontinuous small eruptions fed by one or few small-volume magma batches [1]. Generally, these are the most common volcanoes on Earth [2], and form in a variety of tectonic settings, most commonly extensional rifts and/or intraplate transitional zones [3–6]. The size and type of monogenetic basaltic volcanoes depend on volcanic and geomorphological processes, such as type and

duration of eruptions, type and volume of erupted ejecta, type of magma, magma/water ratio if external water available, and eruption rate, as the most fundamental parameters. Depending on these parameters, monogenetic volcanoes can take the form of spatter cones, scoria cones, tuff rings, maars (maar-diatremes), and tuff cones. Typically, monogenetic volcanoes around the world exhibit a great variety of depositional characteristics, such as bedded and/or not bedded pyroclastic deposits, sometimes associated with characteristic pyroclastic textures and fragments, which were deposited by fallout or lateral moving pyroclastic density currents during the explosive eruptions. Thus, pyroclastic density currents and/or downstream syn-eruptive tephra remobilization, as well as occasional lava flow emplacement, provides a full architecture characteristic of a monogenetic volcano. In the course of geological time, other external processes have modified the initial edifice of volcanoes; with wind, surface runoff, and whole scale landslides acting as eroding agents on the volcanoes.

Volcanic geoheritage is an important part of the total geoheritage of any region due to the geological processes they demonstrate, the interaction between human societies and nature, and the general fascination of volcanism by humans [7–15]. This heritage element is even more significant from a local to regional perspective within a region where no active volcanism exist [16–19], and well-exposed near-intact original morphology of volcanic geoforms are rare, such as the case in northwest Africa, along the Moroccan Atlas region. Proper documentation of the morphological features and their core geological aspects can form the center of investigations, including qualitative and quantitative assessment of their role in the geodiversity estimates of a broader region. The relative rarity of such volcanic geoforms within a region naturally elevates the geoheritage values of such volcanoes. Here, we provide a morphometric study accompanied with detailed volcano geology approaches to document the rich volcanic geoheritage of the Atlas region within Morocco. Our work can provide the first comprehensive overview of the volcanology of well-preserved monogenetic volcanic landforms in Morocco, and this information can easily be utilized for future geodiversity estimates important in characterizing the values of the land.

In the MAVF field, about 100 monogenetic basaltic volcanic volcanoes have been identified over the past few decades through various scale geological mapping and direct geological research on specific regions. These volcanoes are mostly medium-sized and are represented by scoria cones dominated by Strombolian-style explosive eruptions and maars due to explosive phreatomagmatism. These volcanoes tend to be aligned along a N170° axis over a length of 70 km (Figure 1b). The volcanic products emitted by these monogenetic edifices are mainly pyroclastic deposits and lava flows dominated by alkaline basalts juvenile material, rich in entrapped mantle xenoliths, basanites, nephelinites, and sub-alkaline basalts in subordinate proportion [20].

The first petrographic descriptions of the Middle Atlas volcanism were made by Termier [21], Moukadiri and Kornprobst [22], Harmand and Moukadiri [23], Moukadiri and Pin [24], Natali et al. [25], El Messbahi et al. [26], and Chanouan et al. [27], and they were only interested in documenting and interpreting various ultrabasic enclaves and granulite xenoliths brought to the surface by alkaline basalt flows with an aim to characterize the mantle melt source conditions of the volcanism in this region. As for the first petrological analyses, they were the work of El Azzouzi et al. and Bosch et al. [20,28]. However, few detailed studies have been conducted on the volcanology in this area [29–33]. Among these volcanological works, Amine et al. [31] provided a comprehensive overview of some of the most iconic volcanoes of the field from a geoheritage perspective. Amine et al. [31] provided a good geological overview of only the key volcanoes, but was conducted through a narrative description that does not provide a vocal statement for each known volcano. In this study, we aimed to fill this knowledge gap. Amine et al. [3] also provide general overviews of the best preserved volcanoes, though only based on visual examinations of relevant GoogleEarth satellite images, restricted only for those most iconic sites. Conversely, this study considers each known volcano's basic volcano

geology documentation, and also summarizes basic morphometric parameters, including some new geological observations and classifications. The volcanic geology documentation from the field focuses on a scoria cone complex [29], a maar complex, and a general volcanic geology overview [34], and each is considered in the context of geoeducation and the features of the preserved volcanic geology. Establishing the link between the karstic systems of the basement and the type of phreatomagmatic volcanoes [32], as well as an inventory of the geoheritage values of the region [8], are considered major advances in understanding the volcano geology and geoheritage elements.

The main advance of our work in light of the last five years of volcano geology and geoheritage research of the region, is that it utilizes a systematic method of determining the basic geomorphological characteristics that have not been explored before, including classification schemes applied in other volcanic fields to provide a database that can form a future comparative study of monogenic volcanoes. In this work, new field observations coupled with modern morphometric studies are conducted, with the aim of defining the size and geometry of scoria cones, tuff rings, and maars within the study area.

Morphometry is a statistical and analytical method, which consists of using measurements of the different morphological parameters of volcanoes to identify: erosion rates and relative ages of volcanoes within a region [2,35–41]; the geodynamic context [42–44]; the eruptive styles implied [45,46]; the evolution of the volcanic landscape [38,47,48]; the type of eruption most likely to occur in a region and an assessment of the level of volcanic risk [49,50]; and determine the maximum stresses (σHmax) at the time of volcano emplacement [51–53]. In the latter method, the authors used morphometric parameters to reconstruct magma-fed fractures, as in some cases the extensive coverage of volcanic deposits and lava flows prevents the identification of the substrate and volcano-tectonic structures.

In this study, we have intended to extract the geomorphological parameters of each monogenetic volcano to infer the associated geodynamic context responsible for their generation, tectonic constraints, ejecta morphology and volume, and syn- and post-eruptive processes affecting the volcano.

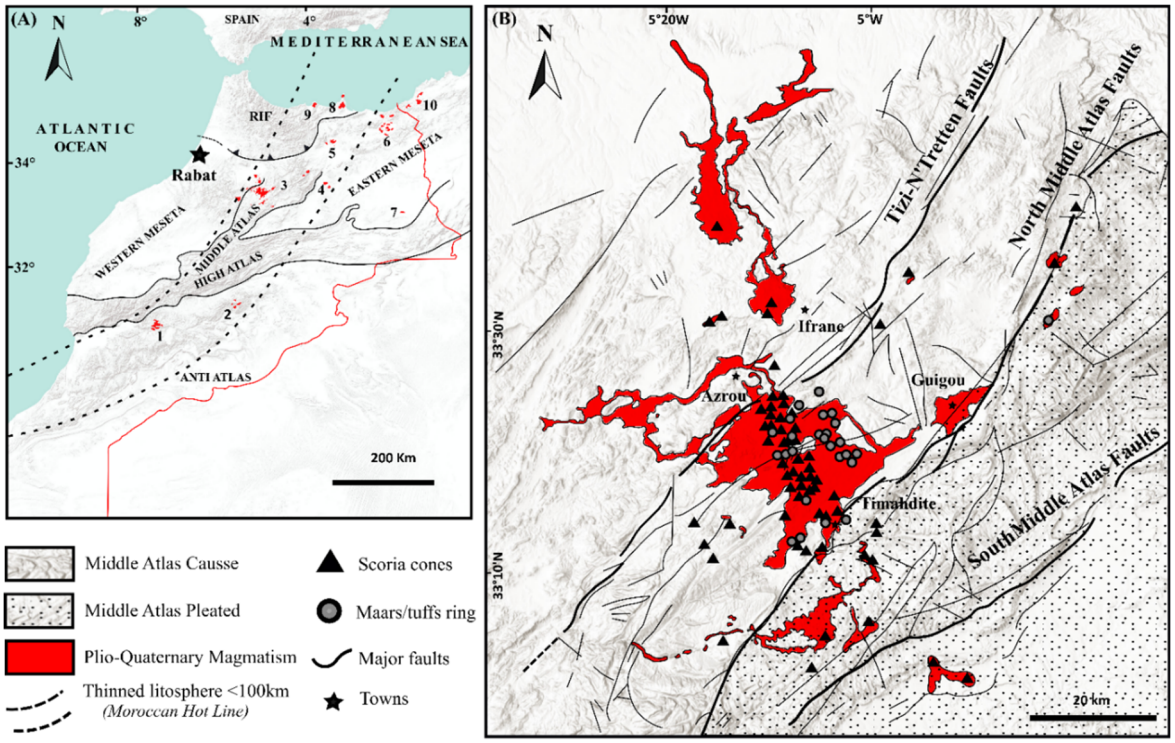

Figure 1. (**A**) Simplified map of Morocco showing the principal structural domains and the thinned lithosphere belt <100 km with volcanism of (1) Siroua, (2) Saghro, (3) Middle Atlas, central Morocco,

(4) Rekkam, (5) Guilliz, (6) Oujda, (7) Tighri, (8) Gourougou, (9) Ras Tarf, (10) and Ouranie (modified from [54,55]); (**B**) Geological map showing the studied volcanoes and the principal geological features of the MAVF (modified from [20]).

2. Geological and Tectonic Setting

In the northwest of the African continent, the Middle Atlas forms the middle geological-geographical domain of Morocco. It is located between the Rif and the High Atlas structural domains (Figure 1a). Indeed, it is limited to the north by the Rif domain; to the west by the Mesetan domain (Western Meseta); to the south by the High Atlas Mountains; and to the east by the High plateaus. The Middle Atlas is an elongated mountain chain, extending over more than 250 km in a general NE-SW direction. This mountain chain consists of a continental basement, structurally impacted during the Hercynian orogeny and their rocks crops, but only in rare structural windows [56,57]. The basement rock are covered by a post-rift sedimentary cover, consisting mainly of Jurassic platform carbonates [58,59], structurally controlled tilted blocks created during the period of Middle Lias-Upper Lias.

The Middle Atlas longitudinally exposes two major structural units, distinguished by the North Middle Atlas Fault (NMAF) [60,61] (Figure 1b):

The Middle Atlasic Causse to the north-west, formed by a set of tabular plateaus with a weakly-folded and more- faulted monotonic relief [62], is made up of mainly carbonate platform rocks of Liassic age; and the Middle Atlas is pleated to the south-east, organized in anticlinal ripples with a Liassic framework separating large synclinal depressions.

The Middle Atlasic Causse is subdivided into two units by the sinistral strike-slip faults trending N40° (Tizi n'Trettene): (i) the Ifrane Causse in the northwest, and (ii) the Guigou Causse in the southeast (Figure 1b); their palaeogeographical evolutions during the first geodynamic period are different and correspond to the period of tectonic stability (lower Lias-middle Lias) [56]. During this period, the evolution of the Middle Atlasic Causse was controlled by different external factors, mainly climatic (biostatic and dry tropical climate). As the eustatic ascent was at the origin of a vertical development of a carbonate tidal platform, a karstic regime developed there with a very reduced terrigenous deposit input and was controlled by internal factors. This is a synsedimentary tectonic scenario recognized within tilted blocks, guided by the late-Hercynian structural elements [56].

Several structural studies carried out in the region showed that during the Eocene period, the presence of NE-SW lateral faults [63] and faults affecting the Hercynian basement during a compressive event [64] were due to the displacement of the Alboran block towards the east of Iberia. These tectonic processes attest to the first major uplift of the Middle Atlas, which continued until the Lower Oligocene [65].

During the period from the Oligocene to Miocene, a NE-SW trending stress field, with a sinistral lateral strike- slip and syn-sedimentary faults trending N120–140, was recorded in conglomerate [65]. In the Upper Miocene-Quaternary, the presence of progressive unconformities in the molasses of Mio-Pliocene age and the Plio-Quaternary conglomerates [65–67] showed that these lithostratigraphic units were affected by N70° E to N90° E dextral faults and N-S sinistral faults. Thus, some studies have shown that the Tizi-N'Tretten fault, which limits most of the volcanoes in the northern region, replayed as a sinistral fault during the Quaternary [64,68], with a compressive stress $\sigma 1$ oriented N140° E to N160° E. This major tectonic event was responsible for the final uplift of the Atlas chains and the folding of its foreland [65,66,69,70] (Figure 2).

These constraints were responsible for the emplacement of the volcanic edifices, which are aligned along a horizontal submeridian direction (N170° on average), with a tectonic shortening in transtension linked to the Europe-Africa convergence [23,56,57,71]. Another explanation is that this shortening is consistent with tectonics and not pure strike-slip movement, such as transtension or even localized extension,

which allow the expression of the mega-tension gap and pull-apart openings, in which the Plio-Quaternary alkaline edifices settle.

The subject of the formation of the Atlas Mountain chains and the appearance of Tertiary-Quaternary volcanoes is still the subject of intense research and debate among authors [54,55,72–79]. Geophysical studies in Morocco highlight the presence of a lithospheric thinning of less than 60 km thickness, and a width of 200–500 km, with an extended NE-SW geometry (Figure 1a).

Several authors [54,72–77,80] attest to the presence of a strong thinning of the lithosphere under the effect of asthenospheric upwelling. This thinning has been shown to cut across not only the structural domains of Morocco, but also the boundary of the Europe-Africa plate. In other words, it affects various geological structures and domains, such as (from north to south) the Massif Central in France, the Eastern Pyrenees, the eastern Iberian margin, the north of the West African Craton, and the Canary Islands. On the Moroccan scale, according to Frizon de Lamotte et al. (2009) [55], the Moroccan Hot Line extends from the western Anti-Atlas, through the central High Atlas, and then through the Middle Atlas, the eastern meseta, and the Rif. This Moroccan Hot Line is associated with recent intraplate volcanism of Tertiary-Quaternary age (Figure 1a).

In the Tertiary and Quaternary alkaline volcanic activity of the Middle Atlas, three episodes can be distinguished [20,28]. The first episode of the Eocene age (35 Ma) is represented by a few very scattered monogenetic volcanoes. The second magmatic episode (16.25 to 5.9 Ma) represents a magmatic event which moved northwards, and new, dispersed volcanic emissions, which were spread throughout the Middle Atlas domain, were simultaneously established with the orogen of the Rif Alpine chains and the uplift of central Morocco. These small volcanoes are largely dismantled and essentially represented by olivine nephelinites (±melilite) and ijolites [81]. Finally, the last episode (3.9–0.6 Ma) is mainly concentrated in the Middle Atlas Causse and groups together the main eruptive centers, including nearly one hundred scoria cones and maars.

Four volcanic manifestations emitted during this last episode are of a much more considerable quantity (about 80 km^3, over an area close to 1500 km^2) including (1) alkaline basalts (58.5%) rich in mantle xenoliths, (2) basanites (22.5%) overlying the alkaline basalts, (3) sub-alkaline basalts (7.8%), and (4) nephelinites (1.2%) [20,82].

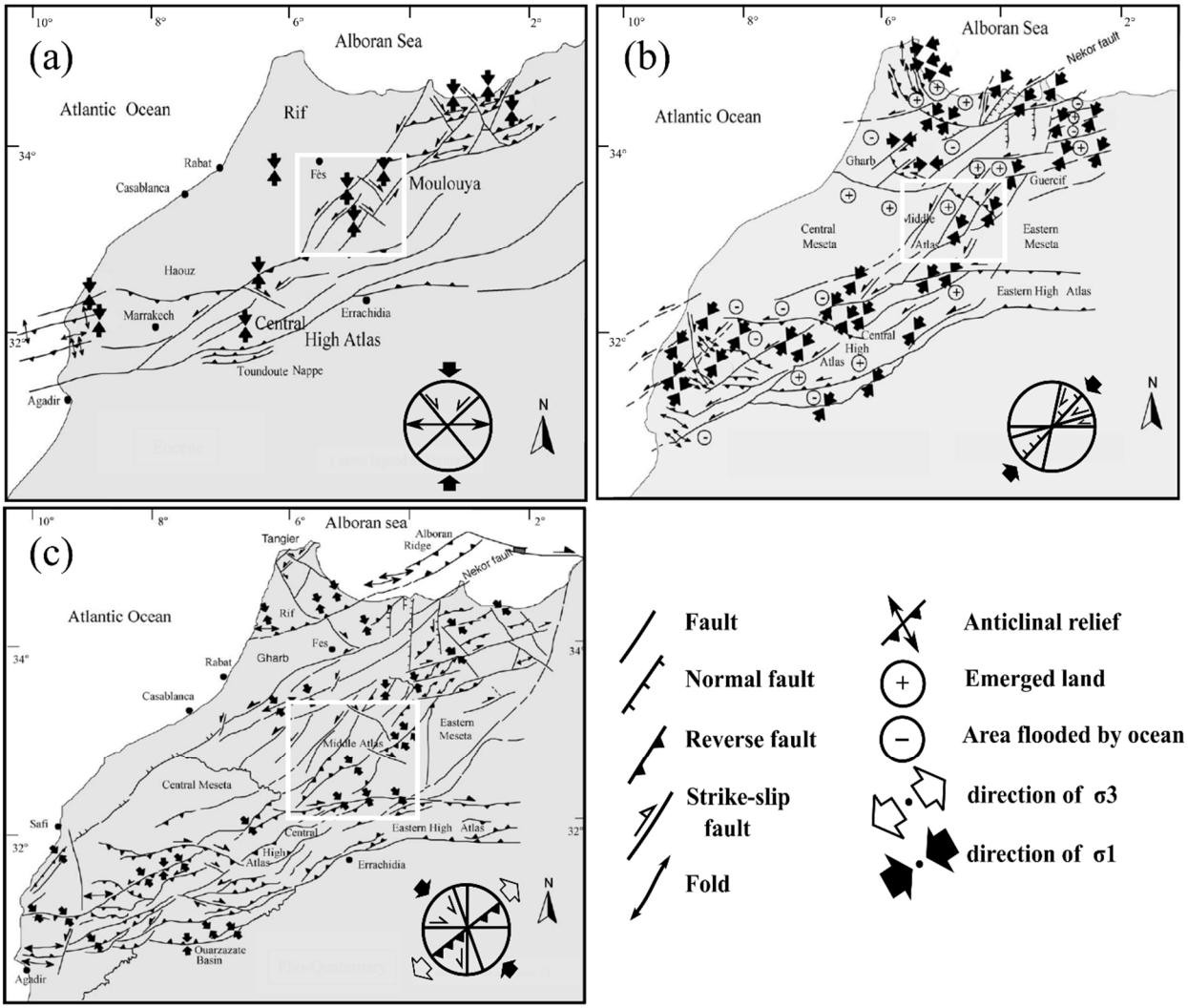

Figure 2. Structural map of Morocco and paleostress directions: (**a**) Eocene; (**b**) Early–Middle Tortonian; (**c**) Plio-Quaternary, the white frame mean to the Middle Atlas area (after [65]).

3. Materials and Methods

In this study, 87 MAVF monogenic volcanoes were analyzed both in the field and in the laboratory, to determine the geomorphometric parameters.

Among these 63 scoria cones, we focused on analyzing 23 unbroken cones, 21 breached cones, and 19 cones were not classified because of almost total degradation. Among the 24 maars, there were 4 maars that were very difficult to identify (Hco) because of degradation by human activity and intense vegetation (e.g., Michlifene maar).

For scoria cones, we used cone height (Hco average) and cone crater diameter (Wcr average) in the same way as defined by Wood [2]. The use of these parameters was aimed at extracting geometric aspect ratios, such as cone height/width (Hco/Wco), and crater width/cone width (Wcr/Wco). Measurements of heights (Hco) and volumes (Vco) were carried out using geological maps, Google Earth, and QGIS software, following the approach by Dóniz et al. [83] (Figure 3). The average slope calculation was carried out by the approach of Hasenaka et Carmichael [84].

The craters (Wcr and Wco) in each field were manually digitized using the add polygon tool in Google Earth, as well as with the interpolation of the satellite images from Google Earth with the ERSI World Hillshade (DEM already processed by the QGIS software providing 30-m spatial resolution) (Figure 3).

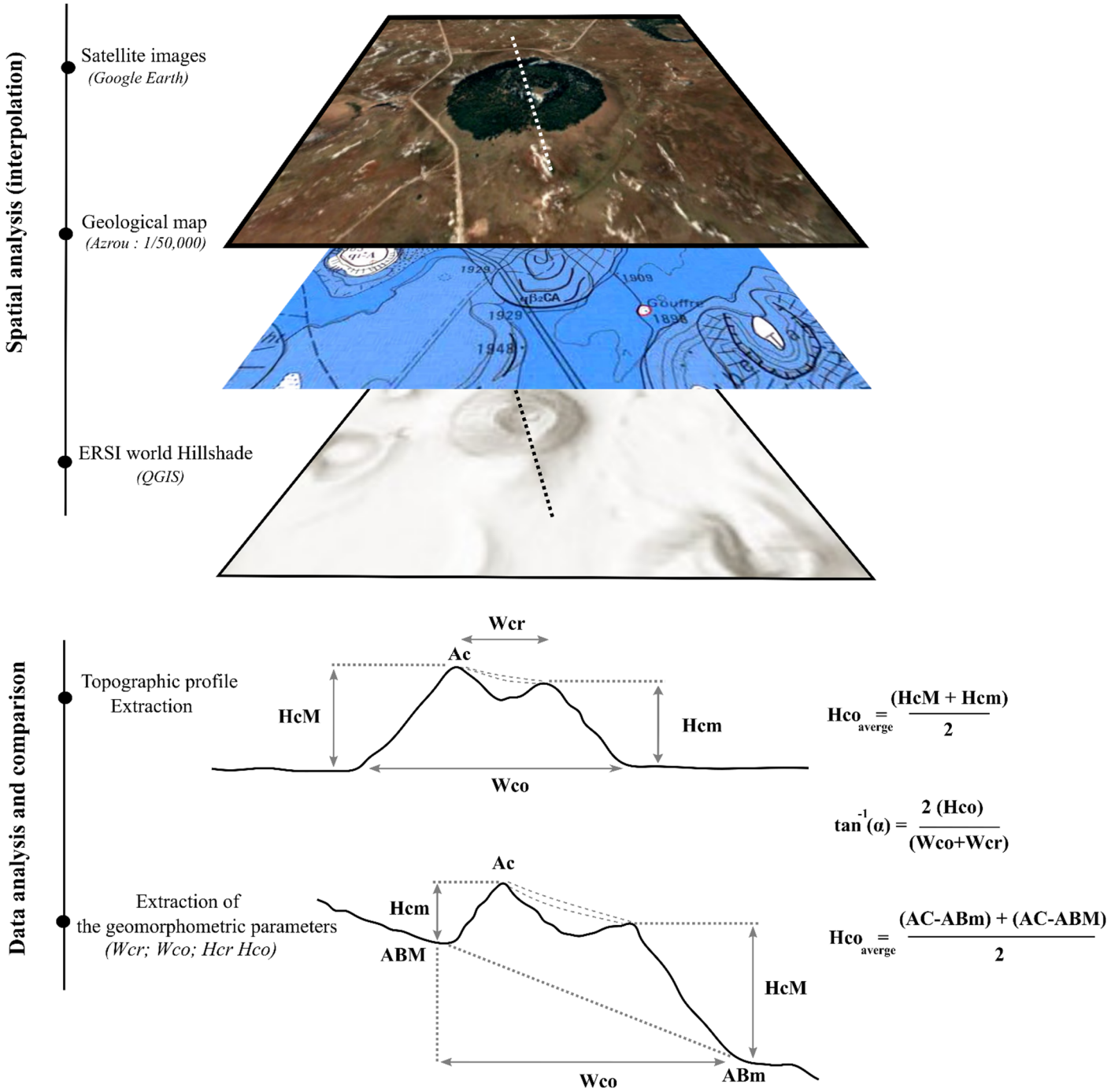

Figure 3. Methods to calculate Hco, Wco, and S° of scoria cones. Following the method of Dóniz et al. [83], where HcM is the maximum height, Hcm is the minimum height, ABm is the minimum altitude of the base, ABM is the maximum altitude of the base, and AC is the altitude of the top of the cone. The calculation of the slope (α) is performed according to the approach of Hasenaka and Carmichael [84].

For the maars/tuff rings, we kept the same method of measuring the geomorphometric parameters of Wco average, Wcr average, and Wcr/Wco, but we tried to find out the maximum theoretical crater depth, the maximum theoretical tephra ring height (Hco), and the difference between these two values. In parallel to the ratios used in this study, we also drew on the work of Graettinger [85] for visible maars identifiable using Google Earth. From the work, crater outline polygons were used to identify the area,

perimeter, and length of the major and minor axes of these monogenic volcanoes (cones/maars) to identify the aspect ratio (AR), elongation (EL), and isoperimetric circularity (IC);

$$AR = (Dminor/Dmajor) \quad (1)$$

$$El = A/\pi\,(Dmajor/2)^2 \quad (2)$$

$$IC=4\pi \times A/P^2 \quad (3)$$

where:

Dminor: is the length of the crater's minor axis;
Dmajor: is the length of the crater's major axis;
A: is the area encompassed by the crater rim;
P: is the perimeter of the crater rim.

For the scoria cones, we analyzed the parameters involved in the configuration of the magma plumbing system and ascent route; for instance, the measurement of the ellipticity and elongation axis of craters, and the crater-breaching bisector. The dominant direction of all these indicators must be analyzed to estimate the maximum compressive stress fields (σHmax). For maars/tuff rings, we treated the different phreatomagmatic apparatuses based on the approach by Paulsen and Wilson [86] and Nichols and Graettinger [87] (azimuthal orientation of regional faults, nearest neighbor analysis, lineation of maars, and their elongations). Regional faults and lineaments were selected within and around studied volcanic fields, based on their proximity, and published literature.

We mapped and manually measured these characteristics for each volcano. As the area does not yet have enough geological data and even age (radiometric), many vent locations are also known only approximately. The method used here is the first whole-scale applied to this area. For recognizing lineaments and visualizing them (not sensu stricto statistically), following this simple method showed up trends and basic links between alignment patterns and major structural element locations. Rose diagrams were then produced for the selected characteristics. Nearest-neighbor analyses on monogenic volcanoes were performed to determine the volcanoes closest to each other. Vents/craters alignments were manually identified based on three or more characteristics and/or craters/cones elongation [52,53,86]. In our work, and according to Paulsen and Wilson [86], we used data to define vent alignments, which were based on observations and were supported by systematic mapping of the positions and elongated forms of volcanic vents.

1. In this case, the alignments are established by drawing a line through the axes of the elongated vents (including circular vents that follow the same pattern);
2. In case the decision between two alignment trends is possible, the elongated events are used to guide this choice;
3. Coalescing cones are mapped as individual vents;
4. In cases where there are no elongated vents, the nearest neighbor method guides the identification of volcanoes that have a small distance between them. The alignment of vents is determined by constructing a trace through the center points of a series of vents.

In nature, scoria cones are usually incomplete (e.g., rarely perfectly circular in map view or having near angle of repose sloped conical shapes, as expected from granular media accumulation) due to breaching, erosion, or recent sedimentary fill. Initial (e.g., primary scoria) cone shape can also be heavily influenced by the present of erosion resistant welded, agglomeratic or clastogenic sequences, especially around the lip of the crater [48,88]. As the elongated shapes of the vents define the orientation of the tectonic stresses and the alignments of the vents, to analyze the vent distribution pattern is a critical step to link magma rise and structural evolution of a region. In this case, it is necessary to systematically define the dimensions and orientations of the axes of the recognized volcanoes' map view (e.g., Dminor and major). The best way to do this is to construct ellipses that best fit the mapped shape of each vent (e.g., the best-fitting ellipse). This has been

systematically measured across all known volcanoes of the region, applying manual tracing of their shapes. As the general geological knowledge about the region's volcano geology is still limited, available geological maps were not suitable to produce this data set in a semi-automated way (e.g., applying pure remote sensing techniques alone). Performing manual or supervised tracing was also beneficial in that we had an interactive way to justify the traces based on the geological observations also made during field works.

We analyzed all these parameters from different approaches, such as field observations, analysis of satellite images available in Google Earth, and ESRI World Hillshade, to arrive at a geomorphological classification of MAVF's monogenic volcanoes, and its setting with respect to the maximum stresses (σHmax).

We used ESRI Hillshade (30 m spatial resolution) maps in combination with Google Earth imagery to manually extract morphometric parameters. In previous work, such morphological data extraction of the volcano geometry has only been conducted in a few iconic sites; hence, our work is a way forward as we provide here a systematic analysis of each known volcanoes of the study area. Small-volume (e.g., monogenetic) volcano morphology has significantly advanced in the last two decades, especially due to the increasing availability of high-resolution digital terrain models (DEM). These techniques commonly use DEMs with a resolution of less than 30 m by applying them on LiDAR (Light detection and ranging) data sources within GIS (Geographical Information System) environments. While these methods are advanced and have led to several novel approaches to monogenetic volcano morphometry, they are heavily reliant on the input data source (DEM) and the statistical capability of the GIS environment; hence, they require specific conditions not commonly available, as in the current study. Conversely, many of these new techniques, while they produce seemingly high-quality data, do not obviously provide more information than traditional parameter-based morphometry, especially in the case of low-resolution DEM and limited knowledge of the volcano geology of the study sites, as was the case in this study. For the purpose of our study, to provide the first comprehensive morphometry study of this volcanic field in combination to extend our geological knowledge of these volcanoes, we kept the method simple and used a supervised manual method with the aid of DEM and satellite imagery to extract morphometric data. This approach can be justified on the basis of (1) the volcanic geology knowledge of the volcanoes is still limited and uneven, despite the excellent recent work from a few iconic sites [31,32]. (2) Exposures are unevenly distributed and the delineation of the boundary of the volcano base is still a complex problem [89,90]; hence, in most cases it still requires supervised manual techniques to justify the polygons in combination with the field records that are also based on spot observations rather than full-scale mappings. (3) The available DEMs that cover the entire field, such as ESRI Hillshade (derived from SRTM) resolution, is 30 m; therefore, interactive tracings of geometric features of each volcano is required to capture the volcano architecture. In addition, the advantage of using ESRI Hillshade is that it provides free access and homogenous coverage of the Earth. Unfortunately, higher resolution DEMs like ALOS-PALSAR do not have full coverage of the volcanic field, despite being 12.5 m in spatial scales. Manual or supervised tracing of volcanic features is also justified based on the difficulty in applying automated feature extractions based on low-resolution DEMs and/or satellite imagery, such as Sentinel data sets. For the purpose of this study, providing the first comprehensive morphometry data set of each volcano of the studied volcanic field with an aim to refine our current understanding of the geoheritage and geodiversity elements of these region, we are convinced that our method is robust, inclusive, and provides a step forward in the next stage of remote sensing-based morphometry and terrain analysis. Basic topographic cross-sections were specifically extracted by following the most characteristic features of the volcanoes, such as elongations (major axis), that generally followed the directions of rupture. The cross sections provided by the first systematic analysis of each of the volcanoes, for the reason of demonstrating their morphological variety and their potential link with the structural models, were sufficient to achieve this objective.

4. Results

4.1. Morphometric Parameters

Among the 44 cones selected for morphological analysis, 23 were unbreached, 21 were breached, and 19 were not classified (Table 1 and Figure 4). Due to intense erosive factors, the shape of volcanoes can be completely transformed. From these factors, it is not straightforward to find the link between various measured geomorphic parameters and the geological cause responsible for generating them.

Table 1. The morphometric parameters of the scoria cones of MAVF (the GPS coordinates refer to the center point of the volcano). Asterix marks no data.

Genre	Scoria Cones	GPS Coordinate	Hco (m)	Wco (Average)	Wcr (Average)	Hco/Wco	Wcr/Wco	S (°)	AR	EL	IC	V (km³)
Unbreached cone	Hebri	33° 21′ 35″ N; 5° 8′ 26″ W	151	1545	483	0.10	0.31	16	0.97	0.95	0.98	0.46
	Tahabrite (T 1)	33° 20′ 37″ N; 5° 7′ 46″ W	74	970	533	0.08	0.55	19	0.66	0.65	0.91	0.10
	Chmil Assou	33° 16′ 49″ N; 5° 7′ 22″ W	25	702	330	0.03	0.47	7	0.57	0.60	0.82	0.02
	Boutagarouine (B 3)	33° 16′ 43″ N; 5° 5′ 44″ W	120	1260	773	0.10	0.61	26	0.81	0.63	0.81	0.29
	Boutagarouine (B 4)	33° 17′ 2″ N; 5° 5′ 14″ W	105	928	448	0.11	0.48	24	0.90	0.89	0.98	0.13
	Boutagarouine (B 5)	33° 17′ 17″ N; 5° 5′ 37″ W	69	970	650	0.07	0.67	23	0.86	0.66	0.82	0.12
	Boutagarouine (B 6)	33° 17′ 11″ N; 5° 4′ 54 ″ W	23	620	298	0.04	0.48	8	0.72	0.71	0.93	0.01
	Tabourit	33° 10′ 51″ N; 5° 15′ 6″ W	93	1140	268	0.08	0.23	12	0.84	0.82	0.94	0.16
	El koudiat (K 1)	33° 31′ 53″ N; 5° 9′ 19″ W	59	598	295	0.10	0.49	21	0.82	0.53	0.83	0.04
	Rabouba	33° 14′ 21″ N; 5° 7′ 56″ W	84	558	108	0.15	0.19	20	0.95	0.94	0.97	0.03
	Mijmouane	33° 23′ 10″ N; 5° 10′ 3″ W	48	735	236	0.06	0.32	11	0.29	0.34	0.54	0.03
	Am Larays	33° 1′ 51″ N; 4° 53′ 24″ W	138	1175	363	0.12	0.31	19	0.71	0.70	0.93	0.27
	Ouaoussentecht	33° 35′ 42″ N; 4° 40′ 54″ W	93	1515	910	0.06	0.60	17	0.77	0.69	0.92	0.34
	Aguelman Sidi Ali	33° 5′ 7″ N; 4° 59′ 45″ W	61	876	235	0.07	0.27	11	0.81	0.86	0.94	0.06
	Tichniouine	33° 18′ 29″ N; 5° 5′ 40″ W	36	445	222	0.08	0.50	18	0.57	0.59	0.77	0.01
	Masrabe	33° 14′ 32″ N; 5° 2′ 41″ W	29	430	270	0.07	0.63	20	0.81	0.83	0.97	0.01
	Habri	33° 23′ 00″ N; 5° 9′ 23″ W	91	1215	622	0.07	0.51	17	0.83	0.79	0.96	0.20
	H3	33° 23′ 00″ N; 5° 9′ 23″ W	28	661	267	0.04	0.40	8	0.69	0.71	0.91	0.01
	Chtifat (C 1)	33° 18′ 42″ N; 5° 8′ 6″ W	110	1470	513	0.07	0.35	13	0.69	0.67	0.91	0.29
	Chtifat (C 2)	33° 17′ 45″ N; 5° 7′ 44″ W	16	920	533	0.02	0.58	5	0.77	0.76	0.91	0.02
	Lachmine Lakbir (LA 1)	33° 11′ 42″ N; 5° 6′ 42″ W	51	730	265	0.07	0.36	12	0.98	0.86	0.97	0.04

	Ait Quassou	33° 11′ 32″ N; 5° 4′ 5″ W	12	515	217	0.02	0.42	5	0.84	0.76	0.93	0.005
Breached cone	Lachmine Izyar	33° 15′ 54″ N; 5° 6′ 39″ W	105	1155	727	0.09	0.63	26	0.97	0.95	0.97	0.21
	Tahabrite (T 2)	33° 20′ 51″ N; 5° 7′ 37″ W	75	765	490	0.10	0.64	28	0.75	0.67	0.94	0.07
	Tahabrite (T 3)	33° 20′ 49″ N; 5° 7′ 14″W	19	440	238	0.04	0.54	10	0.86	0.81	0.95	0.01
	Boutjatiout	33° 21′ 45″ N; 5° 6′ 58″ W	74	863	363	0.09	0.42	16	0.73	0.74	0.95	0.08
	Boutagarouine (B 2)	33° 16′ 59″ N; 5° 6′ 25″ W	23	913	500	0.02	0.55	6	0.69	0.75	0.93	0.03
	Tichout Tazouggaght	33° 20′ 45″ N; 5° 9′ 39″ W	67	705	180	0.10	0.26	14	0.89	0.84	0.96	0.04
	Tamarakoit	33° 3′ 42″ N; 5° 3′ 58″ W	58	468	213	0.12	0.45	24	0.98	0.88	0.94	0.02
	Tamahrart	33° 30′ 41″ N; 5° 15′ 9″ W	53	594	289	0.09	0.49	19	0.70	0.64	0.93	0.03
	Tizi Idguel	33° 23′ 35″ N; 5° 9′ 33″ W	70	785	300	0.09	0.38	16	0.89	0.88	0.96	0.06
	Selrhert (S 1)	33° 10′ 34″ N; 4° 59′ 35″ W	60	728	363	0.08	0.50	18	0.71	0.70	0.92	0.05
	Selrhert (S 2)	33° 10′ 50″ N; 4° 59′ 56″ W	76	754	339	0.10	0.45	20	0.65	0.68	0.89	0.05
	Ta'issaouit (Ta 1)	33° 19′ 19″ N; 5° 5′ 48″ W	73	883	348	0.08	0.39	15	0.93	0.92	0.98	0.08
	Ta'issaouit (Ta 2)	33° 19′ 5″ N; 5° 6′ 49″ W	52	595	266	0.09	0.45	17	0.79	0.74	0.96	0.02
	Sidi Boundouh	33° 14′ 11″ N; 5° 4′ 37″ W	47	1109	657	0.04	0.59	12	0.62	0.73	0.81	0.09
	Timahdite	33° 13′ 49″ N; 5° 4′ 1″ W	46	457	313	0.10	0.68	33	0.93	0.87	0.95	0.02
	H1	33° 22′ 32″ N; 5° 8′ 47″ W	74	729	412	0.10	0.57	25	0.51	0.60	0.83	0.06
	H2	33° 21′ 50″ N; 5° 9′ 13″ W	29	603	285	0.05	0.47	10	0.99	0.93	0.97	0.01
	Ich Ouaharrouq (IO 1)	33° 24′ 7″ N; 5° 9′ 6″ W	86	1099	436	0.08	0.40	15	0.52	0.58	0.81	0.16
	Ich Ouaharrouq (IO 2)	33° 23′ 54N; 5° 8′ 6 W	54	892	253	0.06	0.28	10	0.56	0.61	0.84	0.05
	Chtifat (C 3)	33° 17′ 51″ N; 5° 7′ 22W	11	514	229	0.02	0.45	4	0.86	0.86	0.96	0.005
	Sud Izyar	33° 14′ 42″ N; 5° 5′ 47″ W	15	674	443	0.02	0.66	7	0.96	0.99	0.97	0.01
Unclassified volcanoes	Azougouash	32° 58′ 21″ N; 5° 8′ 29″ W	*	*	*	*	*	*	*	*	*	*
	Houirt	33° 39′ 11″ N; 4° 36′ 54″ W	*	*	*	*	*	*	*	*	*	*
	Bekrit	33° 3′ 45″ N; 5° 14′ 25″ W	*	*	*	*	*	*	*	*	*	*
	Outgui	33° 38′ 2″ N; 5° 14′ 53″ W	*	*	*	*	*	*	*	*	*	*
	Si Mghid	33° 11′ 45″ N; 5° 15′ 38″ W	*	*	*	*	*	*	*	*	*	*
	Ariana	33° 30′ 59″ N; 5° 14′ 34″ W	*	*	*	*	*	*	*	*	*	*

Ain Kahla	33° 13′ 41″ N; 5° 13′ 9″ W	*	*	*	*	*	*	*	*	*	*
Sidi abdel aziz	33° 15′ 43″ N; 5° 3′ 14″ W	*	*	*	*	*	*	*	*	*	*
Louugnina	33° 0′ 39″ N; 4° 49′ 56″ W	*	*	*	*	*	*	*	*	*	*
Talsast	33° 13′ 43″ N; 5° 16′ 54″ W	*	*	*	*	*	*	*	*	*	*
Lachmine N′kettane (LK 1)	33° 22′ 57″ N; 5° 7′ 32″ W	*	*	*	*	*	*	*	*	*	*
Lachmine Lakbir (LA2)	33° 11′ 28″ N; 5° 6′ 9″ W	*	*	*	*	*	*	*	*	*	*
Ali ou ahmed (A 1)	33° 13′ 25″ N; 4° 58′ 13″ W	*	*	*	*	*	*	*	*	*	*
Ali ou ahmed (A 2)	33° 13′ 25″ N; 4° 58′ 13″ W	*	*	*	*	*	*	*	*	*	*
Ich Ouaharrouq (IO 2)	33° 24′ 18″ N; 5° 8′ 23″ W	*	*	*	*	*	*	*	*	*	*
Ras Elma	33° 27′ 4″ N; 5° 8′ 57″ W	*	*	*	*	*	*	*	*	*	*
El koudiat (K 2)	33° 31′ 2″ N; 5° 9′ 47″ W	*	*	*	*	*	*	*	*	*	*
Regada	33° 31′ 13″ N; 4° 58′ 0″ W	*	*	*	*	*	*	*	*	*	*
Dayat Yfrah	33° 34′ 24″ N; 4° 56′ 8″ W	*	*	*	*	*	*	*	*	*	*

*: no reliable data.

A total of 20 maars were selected for geomorphological analyses. Regarding the remaining maars, either the periphery of the cone could not be identified because of the dense vegetation (case of the Michlifene maar), or the periphery of the cone was degraded by human activity (case of the Tajine maar). Among the 20 maars selected for the morphological analysis, 15 of them had a closed crater (e.g., Lachmine Lakbir et Sghir), while 5 of them had an open crater, such as Tit Ougmar, Boubalghattene, Touna (Figure 5).

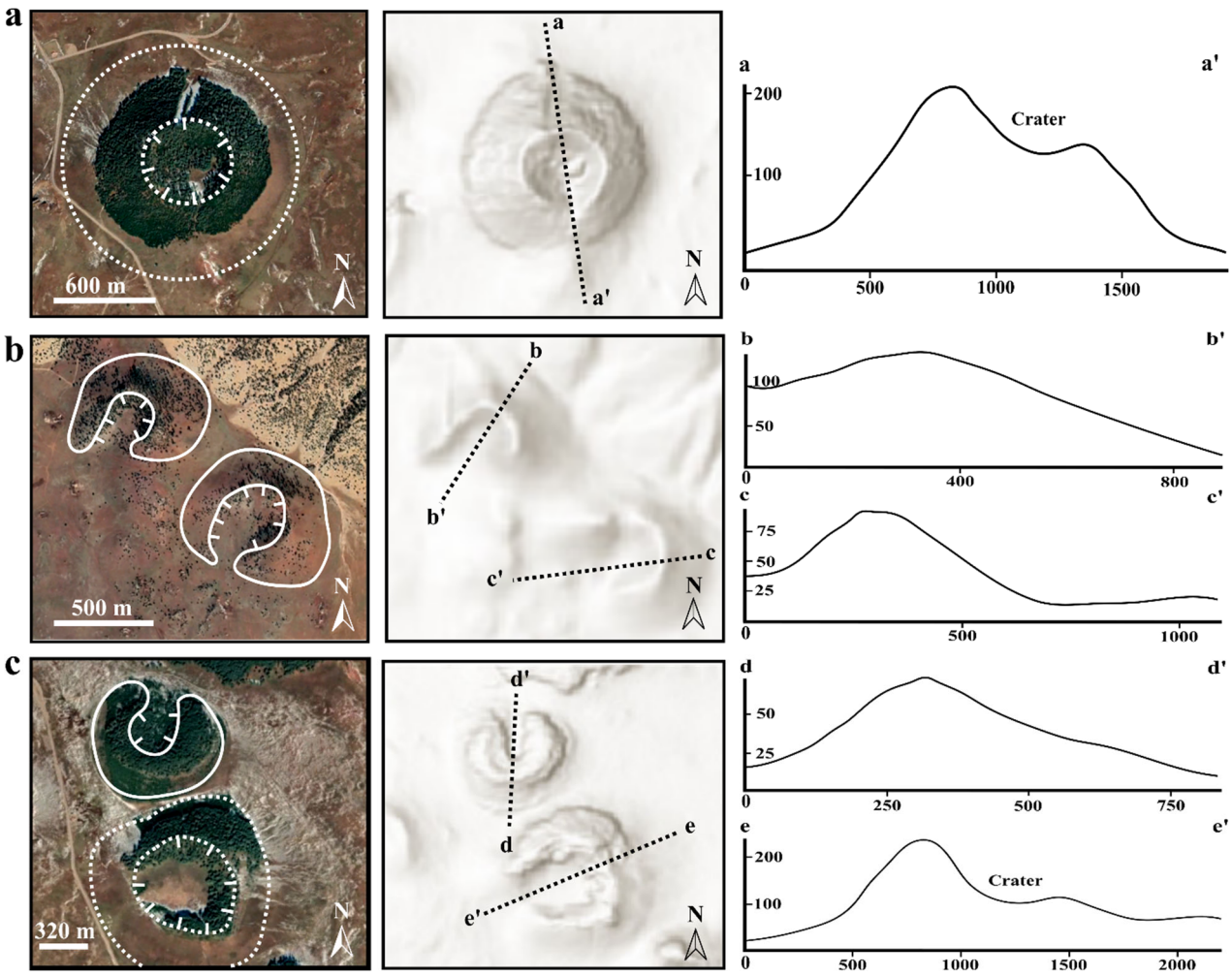

Figure 4. Google Earth satellite photos, digital terrain models, and associated topographic profiles along the dotted lines for scoria cones: (**a**) Hebri (33° 21′ 35″ N; 5° 8′ 26″ W); (**b**) Selrhert (S 1 and 2) (33° 10′ 33″ N; 4° 59′ 35″ W et 33° 10′ 51″ N; 4° 59′ 56″ W); (**c**) Habri (33° 23′ 00″ N; 5° 9′ 24″ W), Tizi Idguel (33° 23′ 35″ N; 5° 9′ 33″ W).

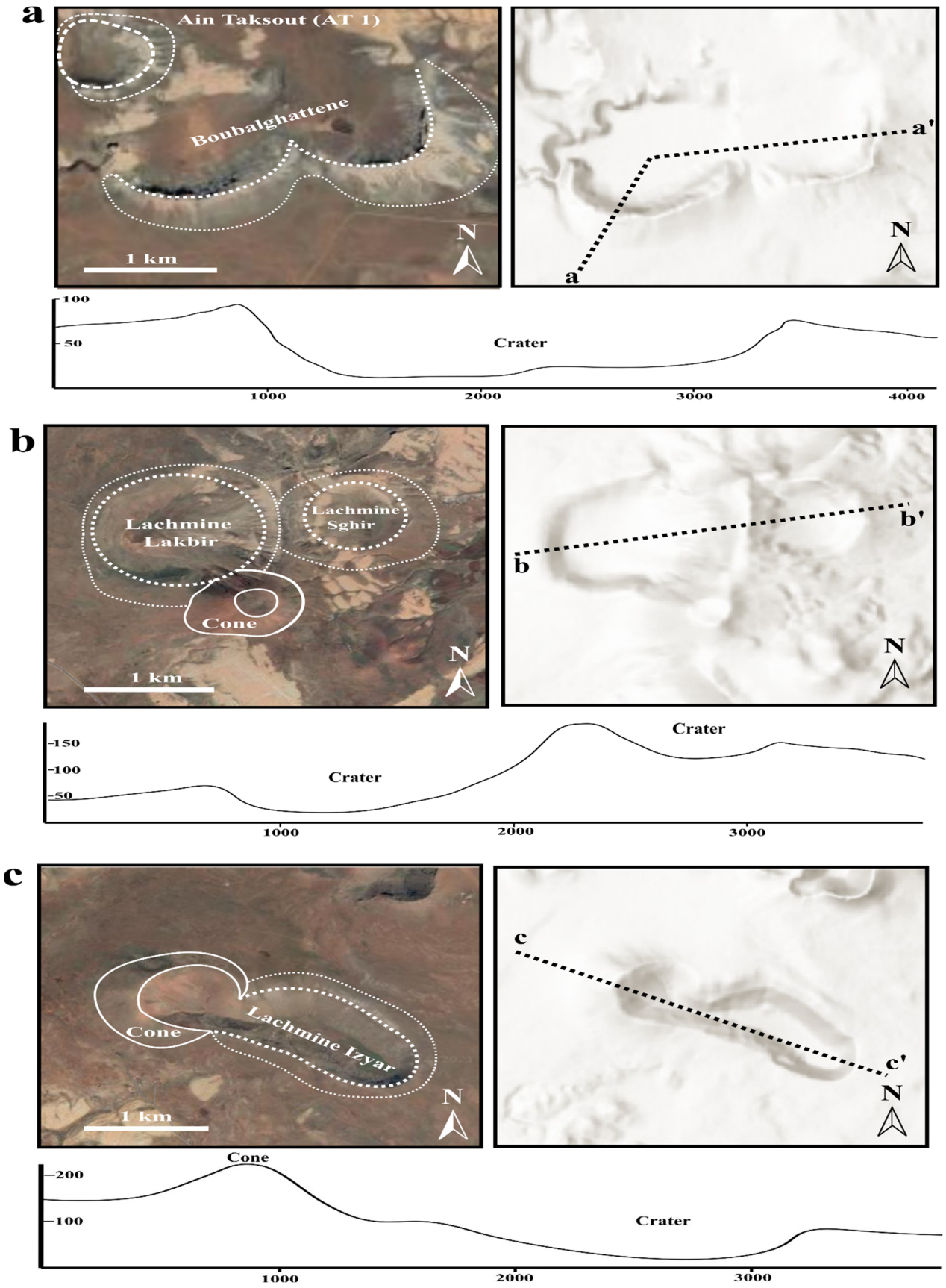

Figure 5. Google Earth satellite photos, digital terrain models, and associated topographic profiles along the dotted lines for maars: (**a**) Boubalghattene (33° 20′ 33″ N; 5° 2′ 56″ W); (**b**) Lachmine Lakbir et Sghir (33° 12′ 19″ N; 5° 7′ 7″ W et 33° 12′ 26.312″ N; 5° 6′ 15.023″ W); (**c**) Lachmine Izyar (33° 16′ 0″ N; 5° 6′ 14″ W).

4.1.1. Crater diameter, AR, IC, and EL

Scoria Cones

The crater area of 44 scoria cones average 0.0013 km^2, with perimeters ranging between 0.34 and 2.8 km. Morphometric parameters, as recorded in Table 1, show that the average diameters of the major and minor axes of the craters are 438 m and 33 5 m, respectively. The major axis measurements reach up to 1300 m, and the minor axis measurements reach 790 m. The smallest crater recognized is at the Rabouba scoria cone, with an average diameter of 108 m. The largest crater is measured at Ouaoussentecht scoria cone, with an average diameter of 910 m. Dominant proportions of the volcanic cones' craters (44%) have diameters that fall between 600 and 800 m (Figure 6a).

In general, the craters in the database have a wide range of aspect ratio (AR) and elongation (El). The craters have an average aspect ratio of 0.78, with 52% of the values between 0.80 and 1, and 30% between 0.65 and 0.80. Only 11% of scoria cones have an equant shape (>0.95); e.g., the cone of H2, Hebri, Tamarkoit, and Rabouba (Figure 6b). The craters have bounded with a relative isoperimetric circularity, with an average value of IC = 0.9, and 75% of the cones have a value between 0.9 and 1 (e.g., Hebri, H2, and Ta'issaouit) (Figure 6c). The elongation has an average of 0.75, and 14% of the cones represent a higher elongation value of 0.92 (e.g., Hebri cone and Lachmine Izyar cone). The lower (EL) values of 0.50 represent about 2% of the cone population (Figure 6d).

Maars

MAVF maars are less numerous (29%) than scoria cones (71%) and are mainly concentrated in the Tabular Middle Atlas. These maars have relatively diverse morphometric characteristics, as shown in Table 2 below.

Table 2. The morphometric parameters of the maars of MAVF. Avec (MTCD) maximum theorical crater depth; (MTRH) maximum theorical ring height. Asterix marks no data.

Maars/Tuff Ring	GPS Coordinate	MTCD (Depth)	MTRH (Hco)	MTCD-MTRH	S (°)	Wco	Wcr	AR	EL	IC	V (km^3)
Lachmine Ouazdem	33° 20′ 60″N; 5° 6 ′57″W	37	50	-13	5	923	689	0.71	0.73	0.94	0.08
Ouest Hebri	33° 21′ 28″ N; 5° 9′ 22″ W	65	24	41	20	730	612	0.88	0.90	0.97	0.06
Tit Ougmar	33° 19′ 22″ N; 5° 8′ 53″ W	65	35	30	22.5	858	721	0.63	0.70	0.91	0.09
Aadouche	33° 19′ 20″ N; 5° 8′ 11″ W	47	20	27	17.5	955	720	0.76	0.76	0.95	0.09
Touna	33° 19′ 45″ N; 5° 7′ 43″ W	46	30	16	10	703	453	0.73	0.75	0.95	0.03
Lachmine Izyar	33° 16′ 1″ N; 5° 6′ 14″ W	128	30	98	15	1373	1115	0.46	0.53	0.76	0.32
Lachmine Sghir	33° 12′ 26″ N; 5° 6′ 15″ W	75	28	47	15	1140	802	0.93	1.00	0.98	0.13
Lachmine Lakbir	33° 12′ 19″ N; 5° 7′ 8″ W	170	20	150	12.5	1595	1430	0.99	0.90	0.97	0.63
Timahdite	33° 14′ 1″ N; 5° 4′ 9″ W	22	62	-40	20	1012	800	0.60	0.40	0.84	0.13
Lachmine Ouanou	33° 19′ 33″ N; 5° 2′ 16″ W	46	18	28	10	1380	973	0.79	0.75	0.96	0.22
Lachmine Ait ben Qassou	33° 19′ 35″ N; 5° 2′ 48″ W	29	15	14	10	934	693	0.89	0.83	0.97	0.08
Lachmine Ghaline	33° 19′ 06″ N; 5° 1′ 34″ W	36	25	11	15	732	590	0.76	0.75	0.96	0.05
Lachmine Tajine	33° 19′ 46″ N; 5° 1′ 14″ W	totally demolished by human activities			*	1115	849	0.78	0.77	0.94	0.15
Boubalghattene	33° 20′ 33″ N; 5° 2′ 55″ W	51	30	21	10	1435	920	0.97	0.81	0.97	0.19
Ahfour Ouhadane	33° 20′ 24″ N; 5° 3′ 45″ W	82	44	38	24	1530	1250	0.74	0.77	0.95	0.44
Ain Taksout (AT 1)	33° 20′ 52″ N; 5° 4′ 11″ W	60	6	54	20	909	655	0.88	0.85	1.00	0.07
Ain Taksout (AT 2)	33° 21′ 25″ N; 5° 4′ 2″ W	22	12	10	15	1240	851	0.90	0.88	0.97	0.15
Ben Said (BS 1)	33° 22′ 38″ N; 5° 3′ 1″ W	50	40	10	*	1420	780	0.30	0.47	0.29	0.12
Ben Said (BS 2)	33° 22′ 59″ N; 5° 3′ 21″ W	59	34	25	17	863	660	0.81	0.84	0.97	0.07
Lachmine n'Ait Lhaj	33° 23′ 2″ N; 5° 4′ 18″ W	110	65	45	25	1390	880	0.94	0.89	0.94	0.16
Masrabe	33°14′3″N; 5° 2′ 13″W	54	25	29	15	556	418	0.90	0.89	0.97	0.02
Lachmine N'kettane (Ln 1)	33° 22′ 42″ N; 5° 7′ 35″ W	104	73	31	22.5	1380	938	0.66	0.72	0.93	0.20

Lachmine N'kettane (Ln 2)	33°23′17″N; 5° 7′ 9″W	totally destructed by erosion			*	395	296	0.87	0.85	0.97	0.01
Tafraoute	33° 31′ 22″ N; 4° 41′ 29″W	totally demolished by human activities			*	1400	983	0.82	0.75	0.92	0.22
Michlifene	33° 24′ 56″ N; 5° 4′ 49″W	difficult to identify deposits (dense vegetation)			*	*	890	0.76	0.73	0.95	0.17
Boubalghattene-Ahfour Ouhadene	33°20′28″N; 5° 3′14″W	51–58	30–44	21–38	10–24	1980	1683	0.34	0.45	0.66	0.70

*: no reliable data.

In the 24 MAVF maars recognized, their craters represent an average of the two axes (major and minor) between 952 m and 671 m, with major axis measurements coming in at 2510 m, and minor axis measurements at 1420 m. The smallest maar in our baseline data is the Lachmine N'kettane (Ln 2) maar, with an average diameter of 296 m, and the largest maar is the Boubalghattene- Ahfour Ouhadene composite maar, which has an average diameter of 1683 m (Figure 6e). Most maar craters (71%) are 0.6 to 1 km in diameter. The craters have an average area of 0.56 km^2, with perimeters ranging from 0.9 to 6.5 km.

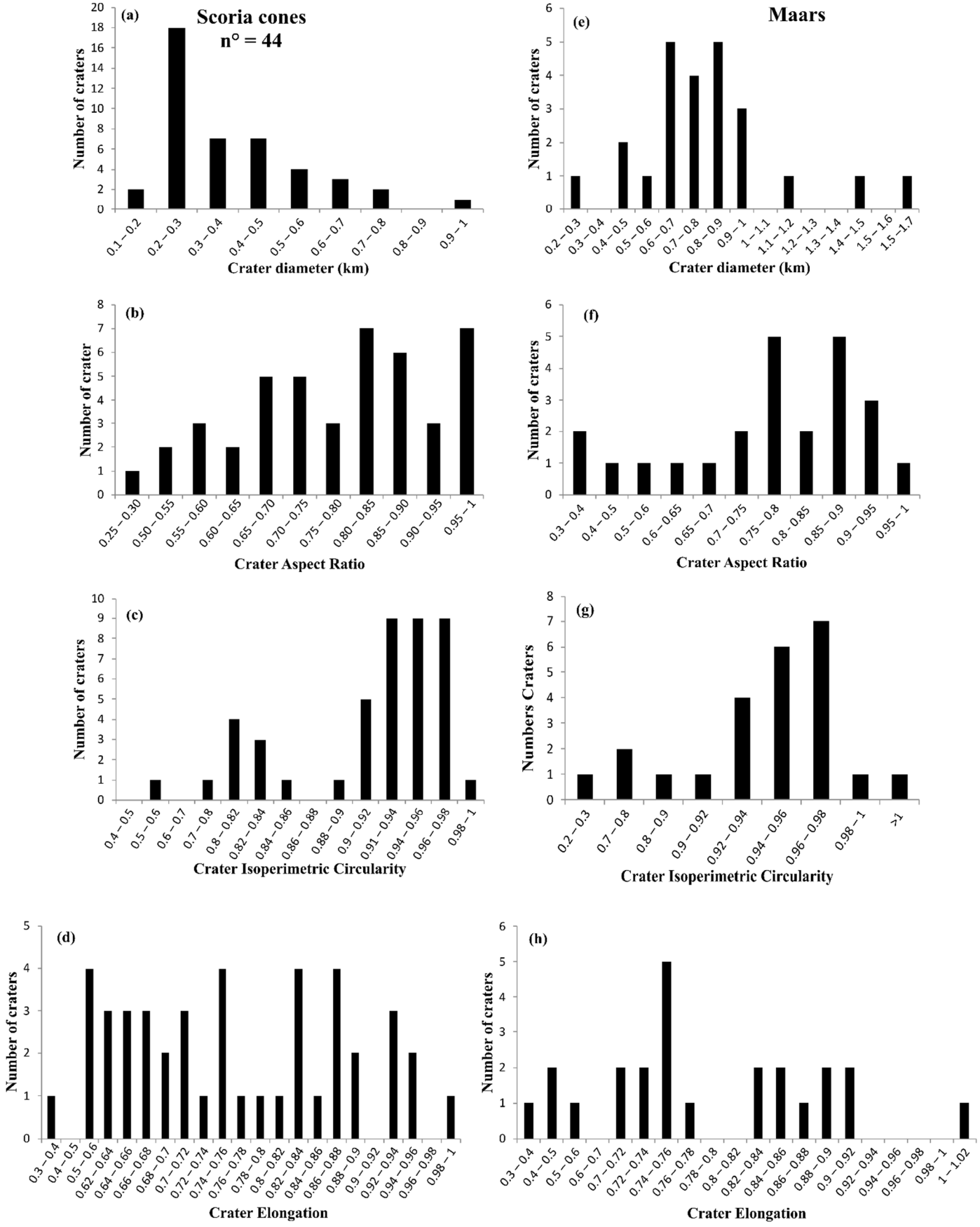

Figure 6. Histograms of craters in MAVF database (Tables 1 and 2) including size, distribution, and shape.

Based on the aspect ratio (AR) data, the maar craters have an average aspect ratio of 0.75, with most values (75%) ranging between 0.70 and 1. The Lachmine Lakbir maar shows a more regular geometry (AR = 0.99) compared to the other MFMA maars (Figure 6f). The craters have limited isoperimetric circularity and correspond to an average value of 0.90. About 71% of the maars have a value between 0.92 and 1 (Figure 6g). The mean of the elongation values of the maars is 0.75, with a maximum value E1 = 0.92 for Lachmine Sghir. The elongation of the maars has an average of 0.75, with the maar of Lachmine Sghir showing the higher elongation value (EL = 0.92). The values of EL below 0.60 represent about 17% of the maars (Timahdite, Ben Said, Lachmine Izyar, and Boubalghattene-Ah-four Ouhadene) (Figure 6h).

4.1.2. Hco/Wco, Wcr/Wco, and S (°) /Hco/Wco

1. Scoria cones

Figure 7 shows the geo-morphometric relationship between (Hco), (Wcr), and (Wco). The Hco/Wco ratio is compared to the average ratio of Porter [85] (average Hco/Wco = 0.18), and the maximum ratio of Settle [36] (Hco/Wco = 0.2). The average Hco/Wco ratio of studied cones is 0.07 and has a median value of 0.08 for both breached and un-breached (Figure 7a). The mean Wcr/Wco ratio is 0.45 with a median value of 0.48 for unbreached cones, while the ratio is 0.49 with a median value of 0.47 for breached cones (Figure 7b).

Figure 7a shows that the Hco/Wco ratio = 0.18, and the line Hco/Wco ratio = 0.20 and acts as an upper limit, below which a large dispersion is observed for both types of cones; i.e., the breached and unbreached cones have a very low correlation with the values from Settle and Porter [36,91].

The Wcr/Wco ratio also follows a similar pattern, with unbreached cones (R^2 = 0.45) having a slightly lower ratio than breached cones (R^2 = 0.49) (Figure 7b).

In Figure 7c, a roughly positive linear relationship is noticed for the unbreached (R^2 = 0.52) and breached (R^2 = 0.72) cones. This means that the slope angle increases with increasing Hco/Wco.

2. Maars

For the analysis of Hco vs. Wco, Wcr vs. Wco, and slope vs. Hco/Wcr. The mean Hco/Wco ratio of these phreatomagmatic edifices is 0.031 with a median value of 0.028, and the mean Wcr/Wco ratio is 0.75 with a median value of 0.75 (Figure 7d,e).

Figure 7d shows a dispersion of values with an R^2 value of 0.005. However, a better correlation between Wcr and Wco is observed, with a value of R^2 = 0.84 (Figure 7e). Figure 7 f shows the correlation between the slope and the Hco/Wco ratio of the maars. There is no clear correlation between maars (R^2 = 0.047).

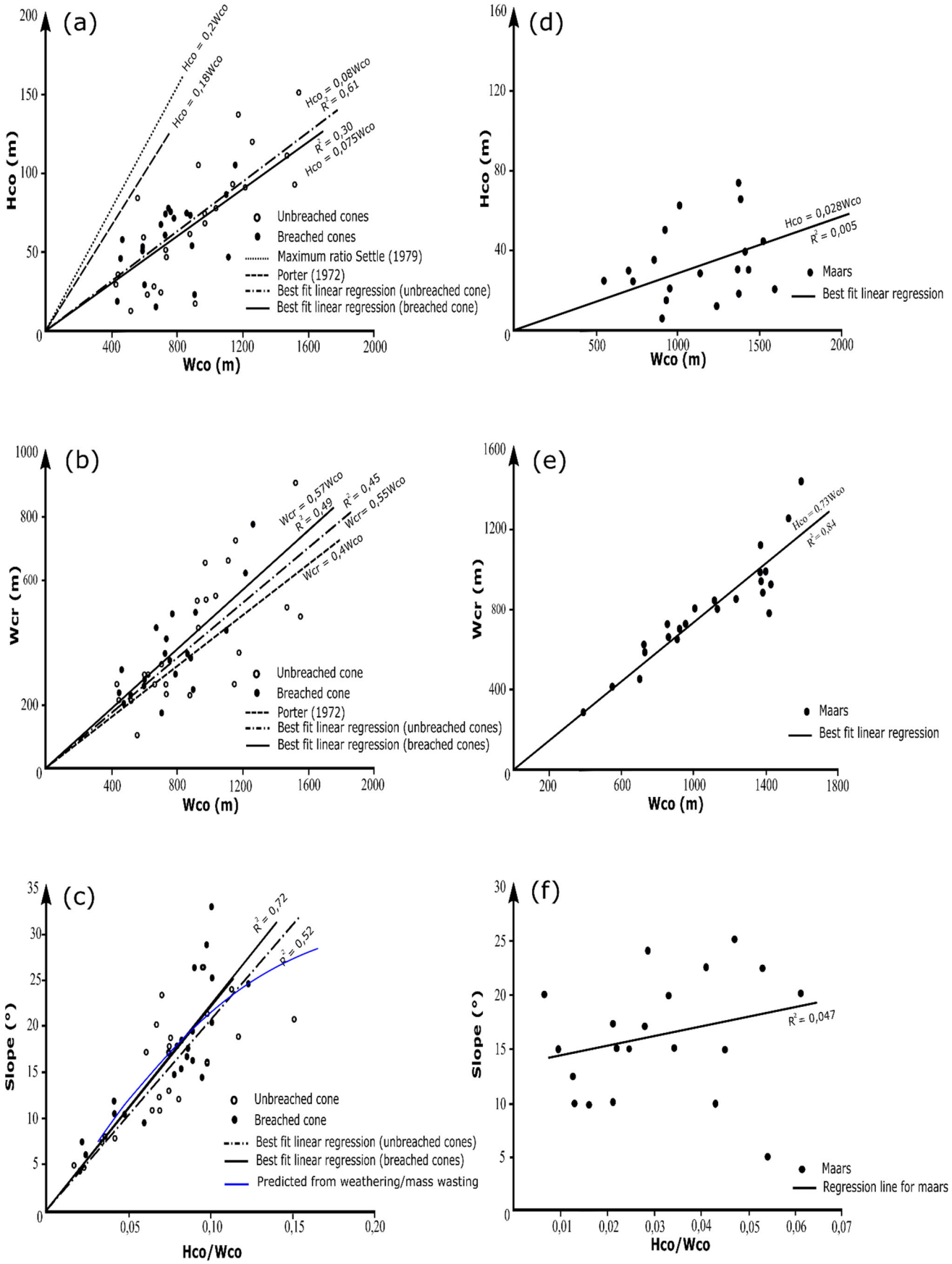

Figure 7. Morphometric relationships for scoria cones (**a**–**c**) and maars (**d**–**f**). Hco: average height, Wcr: crater diameter, Wco: cone diameter.

4.1.3. Stress Field Estimate

The nearest neighbor analysis was performed by the QGIS software. This same software can be used to find out the spatial relationships between the volcanoes to determine which ones are closest to each other. The nearest neighbor analysis of vent distribution pattern recognition within the MAVF made it possible to locate major vent alignments, which have a dominant orientation between N150° and N170°, with some fewer representative orientations according to the N60–80° and N20–40° directions (Figure 8a). As only uneven and limited age data are available from the MAVF, we have not expanded this study to identify spatio-temporal variations (e.g., currently there is not enough high-quality age data to assign lineaments to specific ages). Concerning the faults, the data from the studied region show a main orientation in the N40–50 ° direction, with few orientations in the N20–40° and N130–140° trends. (Figure 8b).

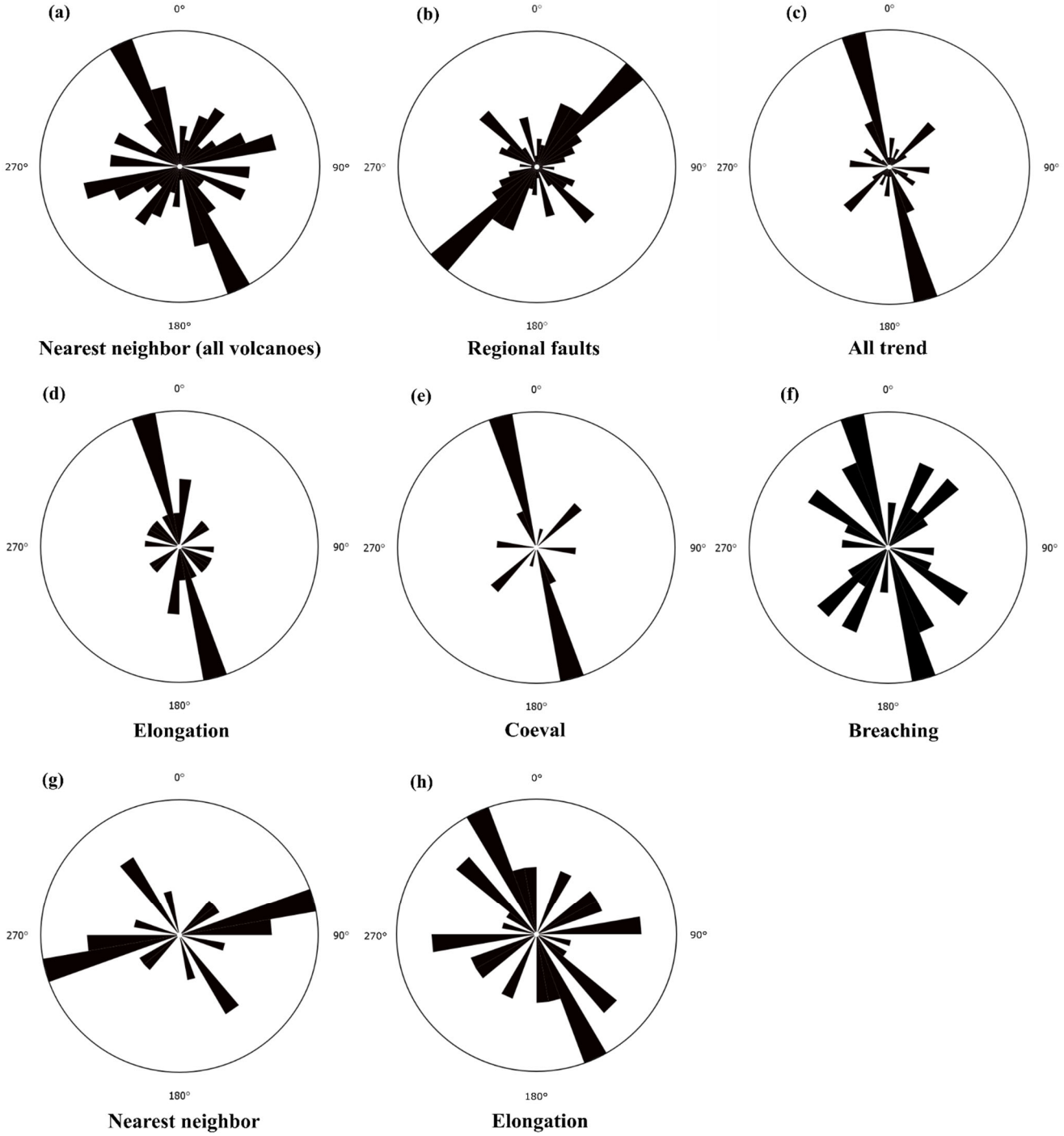

Figure 8. Rose diagrams related to the trend of: (**a**) alignment trend of all volcanoes (cones and maars) in the MAVF, resulting from the nearest neighbour method; (**b**) fault lines from a regional view; (**c**) all of the trend data measured in this study for scoria cones; (**d**) maximum crater elongation axis for scoria cones; (**e**) coeval cone crater alignment for scoria cones; (**f**) breaching bisector azimuth for scoria cones; (**g**) alignment trend of all maars, resulting from the nearest neighbour method; (**h**) maximum crater elongation axis for maars.

The measured parameters that were applied to deduce the geometry of the magma-feeding fractures and to reconstruct the tectonic evolution of the region refer mainly to the character of single edifices and aligned coeval cones, which are concentrated in the Tabular Middle Atlas, are presented in Table 3.

Table 3. Morphometric data of volcanoes in MAVF. Asterix marks no data.

Scoria Cones	Crater Ellipticity Ratio (EL)	Crater Elongation Axis (deg)	Coeval Cones Alignment (deg)	Breaching Bisectors (deg)
Hebri	0.95	*	160	*
H1	0.60	115	160	115
H2	0.93	160	*	345
H3	0.71	160	160	*
Habri	0.79	130	155	*
Tizi Idguel	0.88	*	190	345
Ich Ouaharrouq (IO 1)	0.58	*	225	225
Ich Ouaharrouq (IO 2)	0.61	180	*	180
Mijmouane	0.34	160	160	*
Tahabrite (T 1)	0.65	40	40	*
Tahabrite (T 2)	0.67	*	40	20
Boutjatiout	0.74	300	*	300
Chtifat (C1)	0.67	155	155	*
Chtifat (C2)	0.76	170	165	*
Chtifat (C3)	0.86	*	*	220
Chmil Assou	0.60	*	165	150
Lachmine Izyar	0.95	*	*	120
Timahdite	0.87	230	*	205
Sidi Boundouh	0.73	*	*	230
Masrabe	0.83	160	*	*
Ta'issaouit (Ta 1)	0.92	*	270	270
Ta'issaouit (Ta 2)	0.74		270	210
Tichniouine	0.59	180	*	*
Lachmine Lakbir	0.86	*	160	*
Boutagarouine (B1)	0.83	*	*	150
Boutagarouine (B5)	0.66	90	*	*
Sud Izyar	0.99	*	*	340

*: no reliable data.

The parameters measured show dominant trends between N160° and N70°, with a small number of parameters measured at a few sites indicating N40°, N50°, and N90–100° (Figure 8c). This dominant trend is revealed by three main features: (1) the directions of the axes of maximum elongation of elliptical craters, (2) the direction of aligned coeval vents, and (3) the azimuths of breaches.

The measurement of the direction of crater elongation results in a rose diagram, as shown in Figure 8d, where the dominant axis of crater elongation is N160–170°, with some sites having orientations of N00–10°. Regarding the alignments of coeval cones, the diagram shows a value similar to that of crater elongation (N160–170°), with some trends of N40–50° and N90–100° (Figure 8e).

Breaching depression is one of the most obvious morphological features of monogenic cones, affecting 33% of the MAVF cone population. Examples of scoria cones with breached craters include Tizi Idguel, Ta'issaouit (Ta 1 and 2), Timahdite, Ich Ouaharrouq (IO 1 and 2), H1, H2, etc. The most dominant azimuths of breaching are N160-N170°, followed by less dominant azimuths in the directions N20–30°, N40–50°, and N120–130° (Figure 8f). Most of the breaching bisector azimuth of the monogenic cones is consistent with the orientation of other morphometric features, such as crater elongation, cone alignments, nearest neighbor, etc. The breaching azimuth of the cones shows the relatively same directions in relation to these parameters, in which the direction N160° is dominant.

The Middle Atlas field contains 24 maars with measurable elongations, showing two strong modes in the orientation of the elongation: N150–160°; N130–140°, and N80–90° (Figure 8g). The maar-derived nearest-neighbor data for MAVF show a strong trend of N70–80° and others, i.e. N83–90° and N140–150° (Figure 8h). The Middle Atlas maars show a closely spaced set of craters aligned parallel to strike-slip faults (N70).

4.1.4. Classification by Volume/Diameter of the Recognized Craters

The volume of the cone (Vco) is also obtained by different methods, depending on the shape of the eruptive orifice. In this paper, we estimated the ejecta volume by the calculation method of Dóniz et al. [83], in which:

$$Vco = 1/3(\pi \times Hco)\ ((Wco^2 + Wcr^2) + (Wco \times Wcr)) \quad (4)$$

where, Hco is the mean height of the volcanic edifice, Wco is the cone major diameter, and Wcr is the crater minor diameter.

In addition, we calculated the volume of ejecta of maars as a function of crater diameter by the method of Sato and Taniguchi [92], in which:

$$D = 0.97V^{0.36} \quad (5)$$

Based on the estimated ejecta volume (Table 1), MAVF cones are divided into small to medium, and large cones (Figure 9a,b). It cannot be assessed by the diameter of the crater, since the size of the crater does not reflect the actual size of the cone. Indeed, in nature, there are volcanoes with small craters but large volumes and sizes, and vice versa. In the MAVF, the edifice volume of the scoria cones is less than 0.5 km^3. On a global scale, they are classified as small-volume monogenetic volcanoes (of the order of ~1 km^3 or less) [1].

In general, the volume of scoria cone edifices has an average value of 0.09 km^3, with volumes ranging between 0.0045 and 0.46 km^3. According to the classification scheme of Dóniz et al. [83], monogenic cones are classified as "small", "medium", and "large", depending on the volume: less than 0.01 km^3, between 0.01 and 0.1 km^3, and greater than 0.1 km^3, respectively. The smallest cones, such as Chtifate and Ait Quassou cones, represent 3% of the total cones; the medium cones represent 42% of the MAVF cones; the largest cones represent more than 23% of the total cones (e.g., Jbel Hebri, Ait Bouhou); and 31% of the cones are not classified (Figure 9a,b).

The pyroclastic volume of the maars is estimated at an average value of 0.18 km^3, with volumes ranging from 0.007 to 0.70 km^3 (Table 2). In this case, we have chosen to classify the maars according to the diameter of their craters. The MAVF maars can be subdivided into three categories: three large, three small, and eighteen medium maars according to the classification scheme of Gevrek and Kazanci [93], which classifies a maar as "small", "medium", and "large" according to its crater diameter: less than 500 m, between 500 and 1000 m, and greater than 1000 m, respectively. The largest maars are Boubalghattene, Lachmine Lakbir, and Lachmine Izyar, and the smallest ones are Masrabe, Touna, and Lachmine N'kettane (Ln 2) (Figure 9a,c).

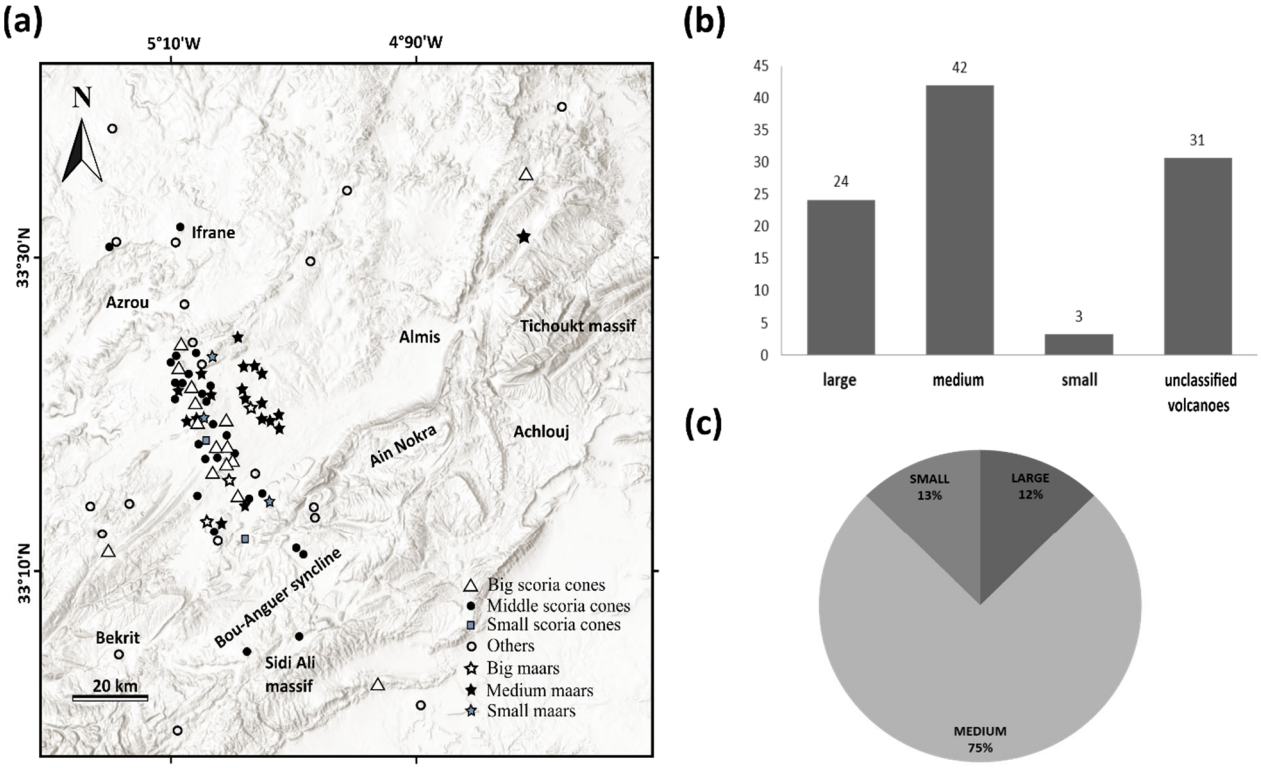

Figure 9. (**a**) Map showing the size distribution of scoria cones of MAVF; (**b**) the distribution of MAVF scoria cones as a function of volume (km^3) according to the approach of Dóniz et al. [83]; (*c*) the distribution of MAVF maars as a function of crater diameter (m) according to the approach of Gevrek and Kazanci [93].

4.2. MAVF Eruptive Products

The studied mafic volcanism covers an area of 1500 km^2 with a total volume of solid products estimated at over 80 km^3 [23], and is responsible for the formation of 87 monogenetic volcanoes in the Middle Atlas, characterized by Hawaiian-style eruptions, mixed eruptions, such as scoria cones formed due to Strombolian-style activity, and phreatomagmatic eruptions, creating tuff rings and maars. In specific well-exposed sites, the tephra succession shows that in some sites, such as Timahdite, the eruption style changed progressively from phreatomagmatic to entirely Strombolian-style magmatic explosive, passing through a transition phase [30] (Figure 10e). These volcanoes have been differentiated according to their topographic, geological, geomorphological, structural, and volcanic evolution. The eruptive material from these eruptions covers most of the Middle Atlas with an estimated cumulative volume of around 80km^3 [44], consisting of pyroclastic fallout, pyroclastic density current deposits, and widely distributed lava flows with diverse surface textures.

4.2.1. Pyroclastic Fall and Pyroclastic Density Current Deposits

Phreatomagmatic eruptions correspond to a very violent explosive volcanic phenomenon, resulting from the interaction of ascending magmas with surface or groundwater in various levels [94–97].

This encounter interacts independently as the magma approaches water; it interacts explosively with groundwater via molten fuel-coolant interaction (MFCI) [93,97–100]. This explosive and direct interaction with magma results in the formation of explosive and monogenic subaerial volcanoes; i.e., built over a short period of time (days to years) [97].

Figure 10. Scoria cones: (**a**) Boutjatiout cone ; (**b**) Ta'issaouit (Ta 2) cone; (**c**) Hebri cone. Maars: (**d**) Lachmine Ghaline maar; (**e**) Timahdite (maar-cone), black arrow shows the pozzolan quarry, white arrow shows the unconformity between the maar and the cone [30]; (**f**) Lachmine N'kettane maar.

Explosive fragmentation of magma and surrounding country rock by explosive interaction between magma and water produced typical pyroclasts and textural features, including abundant cauliflower bombs, intense palagonitisation, bomb sags caused by ballistically ejected dense rocks, syn-eruptive erosional channels, and abundant presence of non-volcanic lithic fragments, all typical characteristics of the pyroclastic successions identified at MAVF. The MAVF is also characterized by frequent magmatic eruptions manifested in the formation of diverse geoforms of scoria cones. In terms of eruptive products, MAVF Strombolian-style explosive eruptions are inferred based on the presence of highly vesicular scoriaceous pyroclasts within fallout deposits. Specifically, the characteristics of the scoria deposits often consist of very coarse, poorly stratified, sometimes red oxidized meter-sized bombs and ballistic blocks. The latter includes irregular shapes and lava spatter-fragments, including: (i) spindle-shaped, (ii) bread-crusted, (iii) cow-pie, (iv) dense bomb, scoriaceous, vesiculated, and (v) ribbon-shaped varieties (Figure 11).

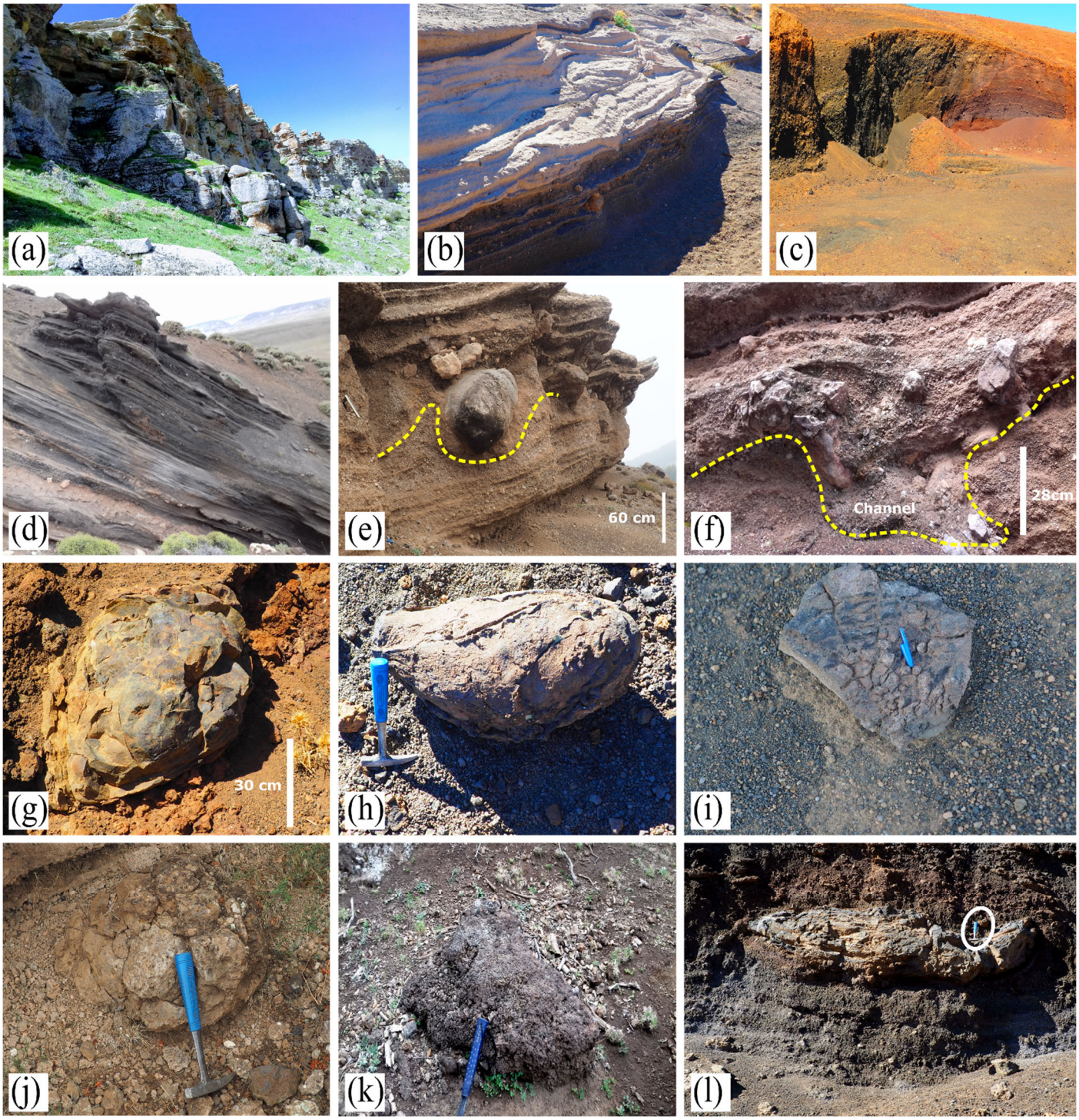

Figure 11. The various texture of pyroclastic deposits and blocks of the MAVF: (**a**) pyroclastic deposit of Boubalghattene maar; (**b**) base surge deposit in the southwestern part of Timahdite volcano; (**c**) pozzolan quarry in the southeastern part of Aguelmam Sidi Ali volcano; (**d**) black scoria deposit in the northern part of Lachmine Lakbir cone; (**e**) load figure in the NNW ring of Lachmine N'kettane maar (Ln 1); (**f**) channel in Lachmine N'kettane maar (Ln 1); (**g**) ellipsoidal ball bomb in the red scoria of Timahdite cone; (**h**) spindle bomb found in the northern part of Hebri; (**i**) bread crust bomb found in the western cone of Hebri; (**j**) cauliflower bomb found in the NNE ring of Lachmine N'kettane maar; **(k)** lava shreds found in the northern part of Lachmine N'kettane cone (Ln 1); (**l**) fragment of clastogenic lava within the black scoria of the cone of Timahdite.

In addition to the variety of magma-type emission products described above, there are also other associated landforms in MAVF formed by lava fountain emissions,

such as spatter fragments and clastogenic lava deposits, which accumulate close to and fall around the vent area (Figure 11l) recording significant heat retention and welding in proximal areas [101,102]. These fragments will be deformed, elongated, flattened like some welded tuffs, and are formed by a mechanism analogous to the welded tuffs of subaerial fallout. From this, formations of spatter deposits, spatter cones, are often formed.

4.2.2. Lava Flow

Pāhoehoe Lava Flow

The pāhoehoe lava flow is characterized by a flat, fragmented, undulating, sometimes corded and ordered surface [103], resulting from a fluid, low viscosity lava. However, it can also form from more viscous magma, with a low effusion rate; therefore, the speed of the lava flow is slow (10 times slower than ʻaā lava flow) [104,105]. The alkaline basalts of the MAVF cover more than 68.5% of the volcanic area, their pāhoehoe lava flows cover a very large area to the west (Oued Tigrigra valley) and to the east (Oued Guigou), thus forming the shield volcano of Jbel Outgui (south-east of El Hajeb). This pāhoehoe lava spreads over the Quaternary deposits of the Sais plain (near Meknes). At the level of the Timahdite volcano, the second effusive phase of the Timahdite strombolian cone is marked by the lava flow at its brecciated base, which covers the cone and descends on the south-eastern flank (Figure 12a). There are many examples of this that require further study.

3. ʻAā lava flow

In contrast, ʻaā lavas have extremely rough and fragmented surfaces, which is more common than pāhoehoe lava on many oceanic islands and continents. In the studied field, ʻaā lava flows are found at the southern flank of the Aguelmam Sidi Ali Strombolian cone, the Lachmine N'kettane (Ln1) cone, and at the northwestern flank of the Ta'issaouit cone (Ta 2) (Figure 12b). In this north-western flank, we observed the transition between the pāhoehoe and the ʻaā flows. This transition was very close to the volcano vent.

The structure and setting of the lava flow in MAVF.

The MAVF presents several structures that generally appear on the flanks of effusive volcanoes, such as lava tubes: this form is developed by a pāhohoe or ʻaā flow-type of a lava which is poor in silica and very hot (1100 and 1200 °C), spreading at relatively high speed (3–50 km/h), on a surface with a low slope <3.5% [106]; comparable with the slope of the limestone bedrock of our volcanic field with an average of between 15 and 20°. This lava is cooled on the surface by the ambient air and on contact with the ground. This forms a solid crust that envelops an inner core that remains fluid, allowing lava to continue to flow downstream [107]. Lava can flow through a tube for several kilometers without being visible from the surface, but sometimes it can become visible due to the collapse of the lava tube roof. In the MAVF, lava tubes can be easily observed in the southwestern part of the Chtifate scoria cone and Aguelmam Sidi Ali volcano, and in the eastern part of Habri volcano [31]. In the field, the main geomorphological signatures used to identify tunnels are hornitos and tumuli [104]. The best hornitos are observed on a very large surface area in the south-western part of Aguelmam Sidi Ali volcano (−10km^2), resulting from flood basalt (Figure 12d–f).

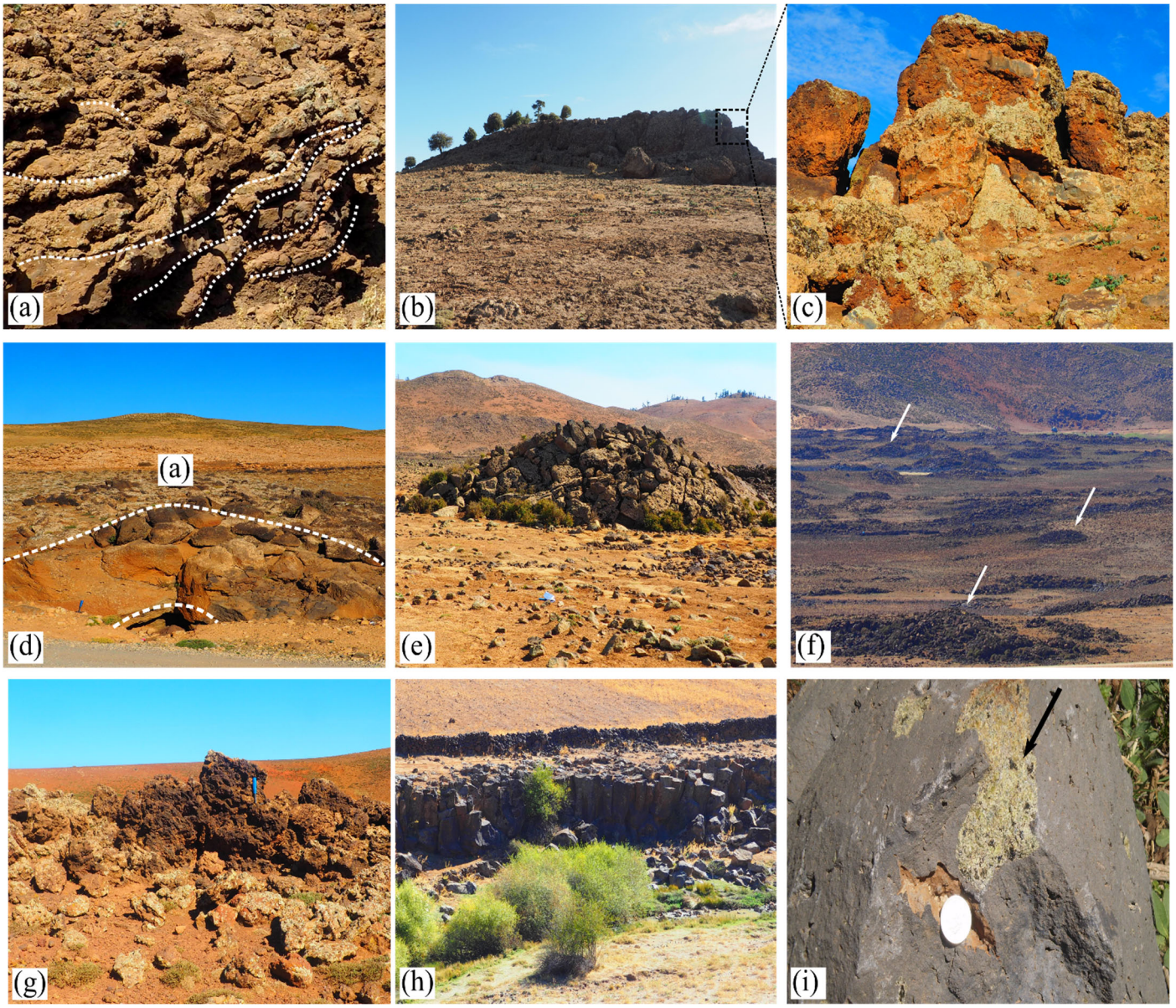

Figure 12. (**a**) The second effusive phase basaltic flow (Pahoehoe) of Timahdite volcano; (**b**) and (**c**) The lava flow 'aā emitted by the Ta'issaouit volcano; (**d**) Tumulus structure found in the southwestern part of Aguelmam Sidi Ali volcano; (**e**) Hornitos structure found in the southwestern part of Aguelmam Sidi Ali volcano; (**f**) The flood basalt of Aguelmam sidi Ali volcano flood basalt, shows several hornitos structures in the southwestern part; (**g**) clastogenic dykes observed in the northern part of Aguelmam sidi Ali volcano; (**h**) the basalt organ outcropping in the Oued Guigou valley; (**i**) blocky lava flow containing olivine xenoliths in the southern part of Lachmine N'kettane volcano.

Other hornitos are observable in the southern part of the Selrhert volcano, and in the eastern part of the Habri volcano. These hornitos are small rootless spatter blisters generated by pressure variation in the tunnel roof [108].

In the northern part of the Aguelmam Sidi Ali volcano, pyroclastic mounds are observed. In some exceptional cases, the mounds show structures resembling lava dykes that vertically intrude into the subjacent lava flow.

Thick and laterally extensive lava fields from MAVF volcanoes commonly exhibit large lava sheets that can be prismatic flows with columnar jointed zones (e.g., basaltic organ). The latter characterizes the exposed volcanoes of the MAVF in two geographical areas. They are frequently observed in the Oued Guigou outcrops in the southern

part of the Timahdite phreatomagmatic volcano and extend along the valley towards the town of Guigou (Figure 12h). Along the eastern side of the Oued Guigou, almost horizontal columns can be seen. Thus, one can observe prismatic flows in the southern and eastern part of the Aguelmam Sidi Ali volcano.

5. Discussion

The Middle Atlas is an intraplate volcanic territory with a wide variety of magma types and eruptive dynamics that give rise to a great diversity of volcanic features and processes. According to the morphological data (AR, EL, IC), the maars such as Lachmine Izyar, Timahdite, Ben Saïd, and Boubalghattene-Ahfour Ouhadene, have AR and EL values lower than 0.6 and IC values lower than 0.9. Such data shows that these volcanoes are composite maars, i.e., multiple superimposed circles. The maars such as Lachmine Lakbir, Lachmine Sghir, and n'Ait Lhaj have a regular crater shape, while the Lachmine N'kettane maar and the Tit Ougmar maar have an elliptical crater shape. Most other maars (64%) range from semi-elliptical to semi-circular. This type of crater shape seems to be similar to what is known as a typical maar shape [85]. As for the scoria cones, Hebri cone, Rabouba, Lachmine Izyar cone, H2, and South Izyar are considered relatively equant volcanic vents (11%). The other scoria cones represent elongated and sometimes composite crater forms such as the Mijmouane cone.

The size of most craters in the MAVF maars, ranging between 600 and 1000 m, is comparable to the statistical data of maars worldwide [85] (Figure 13). However, the size of most cone craters (Wcr) is between 200 to 400 m with a mode of 362 m, and the measure of their basal diameter (Wco) is between 600 to 800 m with a mode of 970 m.

The low Hco/Wco ratio and the considerable increase in the Wcr/Wco ratio of the maars compared to the scoria cones result from the growth mode of the system during the eruption; i.e., the maars have a crater diameter value relatively close to that of the maar cone, and the height is very low compared to the crater diameter and the maar cone (Figure 7d,e).

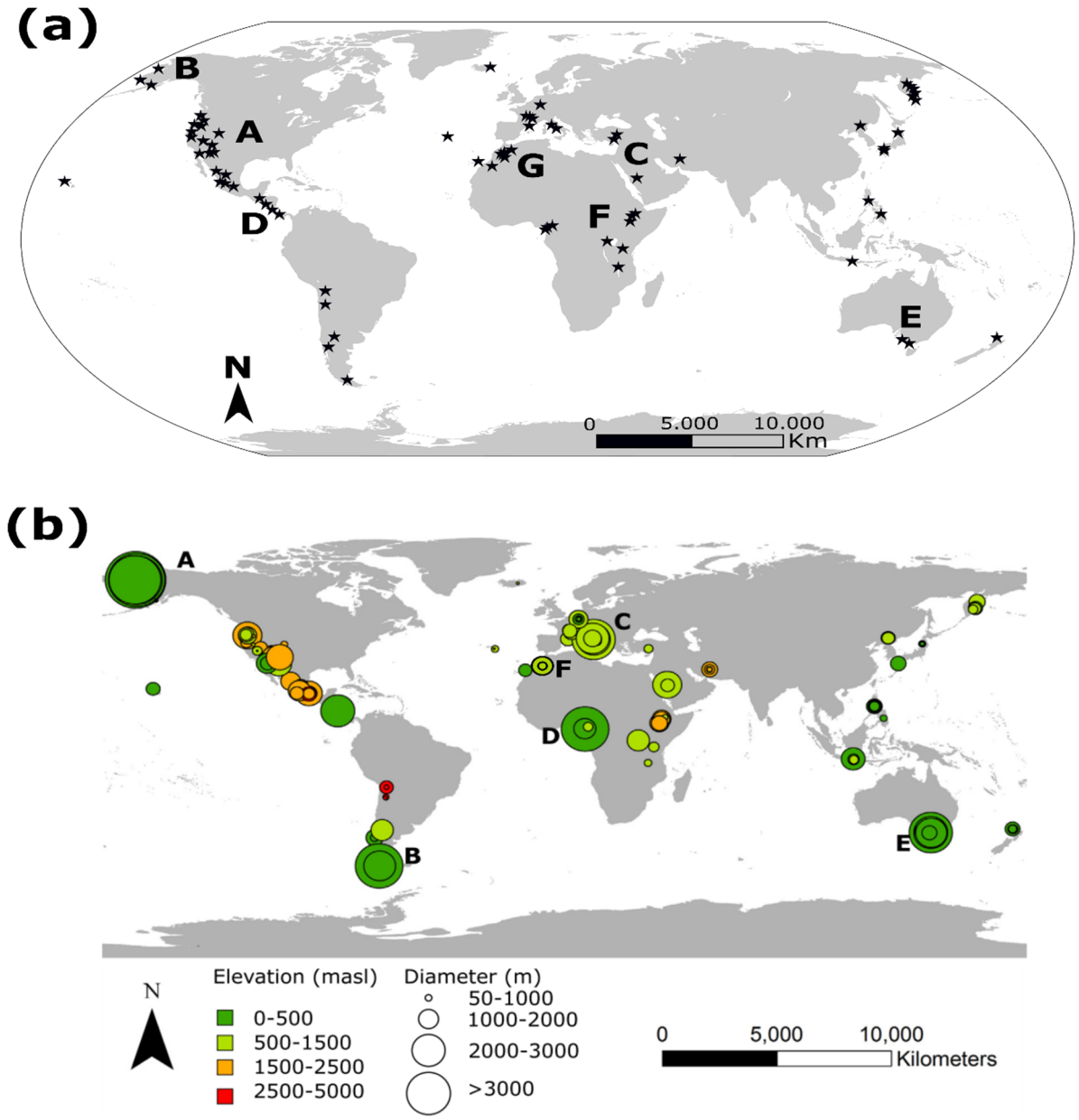

Figure 13. The distribution of maar volcanoes around the world (black stars), we have added the maars of Morocco (modified from [85]): (**a**) (A) Diamond Crater USA, (B) Espenberg Craters on Seward Peninsula AK-USA, (C) Jabal Simagh of the Harrat Kishb field in Saudi Arabia, (D) Nejapa and Ticomo maars in Nicaragua, Lake Leake of Newer volcanic province-Australia, (F) Hora Lake Bishoftu volcanic field-Ethiopia, (G) Middle Atlas- Anti-Atlas and eastern Meseta field volcanoes Morocco; (**b**) Crater size (average diameter) and elevation plotted geographically with one symbol per maar: (A) Espenberg maars, (B) Pali Aike volcanic field, (C) Colli Albani volcanic region, (D) Kumba volcanic field, (E) Newer volcanic province, (F) Middle Atlas volcanic field.

The wide variation in size is controlled by the mode of formation of each type of volcano (magmatic or phreatomagmatic). In previous studies, the enlargement of the phreatomagmatic system is controlled by temperature, magma heat, gas content, viscosity, interaction depth, and the water/magma ratio, which is the main factor in phreatomagmatic fragmentation. Thus, the larger the water/magma contact area, the greater the heat flow, and the more powerful and frequent the explosion. Thus, the succession of phreatomagmatic explosions causes the phreatomagmatic system to increase [99,109,110].

Another important parameter involved in the growth of the phreatomagmatic system and lateral crater growth is the property of the bedrock and regional faults. The nature of

the bedrock plays a very important role in the crater growth of maars, and field studies have shown that unconsolidated rocks can lead to larger diameters [111,112]; whereas, in the studied volcanic field, all the maars are located on limestone bedrock of the Liassic and Eocene age. The only parameter that influences the size of the craters and the variation in the shape of the maars in the Middle Atlas is the distribution and physical state of the water in these limestone beds [85,112–114]. Thus, in our field observations, such as stratigraphy, presence or absence of lithic fragments, accretionary lapilli, and cauliflower bombs, we show several cases of phreatomagmatic to magmatic transition, and vice versa, resulting from variation and depletion of the water source, such as Timahdite (maar-cone) [30], Lachmine Lakbir (maar-cone), Lachmine N'kettane (Ln1) (maar-to-scoria cone), and west of Hebri (scoria cone-to-maar).

The average cone slope angle (~15°) of the MAVF is less than the cone slope (34°) proposed by Wood and Settle [2,36] for recent volcanoes. This MAVF cone slope value is convergent with the average pyroclastic ring slope value of various phreatomagmatic edifices (16°).

The positive linear relationship between the slope of the cones, as a function of Hco/Wco, shows that the slope angle increases with increasing Hco/Wco. However, there is no clear relationship between the value of the slope of the pyroclastic ring and the height of the pyroclastic ring of the maars. The height of the cones is higher than that of the maars, and the Hco/Wco values are relatively scattered, which is due to natural factors such as erosion and / or anthropogenic activities (various human interventions).

The Hco/Wco ratios of the MAVF cones are very low compared to those reported by Settle and Porter [36,91], which means that part of the cone is often characterized by multiple vents or superimposed structures, generating a larger basal extent compared to Hco [115]. Thus, another part of the volcanoes of simple structure has a low Hco/Wco value (e.g., Hebri with Hco/Wco = 0.10). Such a low ratio is mainly due to the degradation of the scoria cones by weathering and by gravity instability over time, which leads to an increase of the basal diameter of the cones and the decrease in height, as well as the reduction in slopes [2]. This is confirmed by Figure 7c, showing a degradation of the cones by weathering and gravity instability leading to a progressive decrease in slope, while degradation of the cones by lava encirclement does not lead to the decrease in slope [2]. Degradation by lava flow inundation is also likely to be played out in the MAVF. The maximum Hco/Wco ratio, with a smaller Wcr (108 m), characterizes the spatter-dominated cone of Rabouba, giving the impression that these are less influenced by erosion processes than the scoria cones. These results are consistent with those mentioned by Wood [2,116]. The degradation of the cones is highly dependent on precipitation and climatic changes over time [2,116]. In the Middle Atlas, the Quaternary is characterized by alternating wet periods on the one hand, and inter-rainy periods on the other hand, characterized by the phenomenon of erosion of relief. The succession of these periods corresponds to the interglacial and glacial periods, respectively [117,118]. From the last glacial period (25,000 cal. BP) until today, vegetation (*Cedrus-atlantica and Pinus halepensis, Pinus pinaster*) has dominated the Middle Atlas .This vegetation cover likely slowed down the erosion of scoria cones during this period. Scott and Trask, and Settle and Wood [2,35,36] used Hco/Wco ratios to calculate the age of volcanoes, proposing that the initial slope value of a young ideal cone is 34° and 35°, and that the slope decreases by 9° per 1 Ma. The use of the Hco/Wco value alone is not sufficient to deduce the relative age because of several parameters that decrease the Hco/Wco ratio, and do not give the exact age of the volcanoes, including:

the nature of the ejecta (fine or coarse) which controls the initial slope of the cones. Spatter-dominated cones have a higher degree of slope than scoria cones and are less affected by erosion than scoria cones.

- gravity instability during frequent eruptions.

- vegetation which can retard erosion; and a very influential parameter added by Favalli et al. [45] concerning the modification of Hco/Wco by the burial of lava, which gives important differences.

The Wcr/Wco values are linearly and positively correlated in both cases (maars and cones), which gives an idea of the strong relationship between crater size and cone size and suggests that the ratio of crater to cone diameter does not change with time through erosional processes. Indeed, this is the case for the San Francisco volcanic field in the U.S. [2,116], the Mauna Kea volcanic field in Hawaii, Lanzarote in the Canary Islands-Spain [115], and the Bayuda volcanic field in Sudan [119].

The extreme value of the morphometric ratio of the Timahdite cone, with an exceptionally high Wcr/Wco (=0.68), can be attributed to the fact that the location of the cone crater rim is controlled by the pre-existing location of the phreatomagmatic crater and its deposit. Thus, cone B5 has an extreme value of Wcr/Wco = 0.66. This value can be attributed to a nesting of several craters, or to this cone being structurally deformed or bound by the burial of the lava flow. Favalli et al. and Kervyn et al. [45,115] denoted that lava flows cover the surrounding terrain or part of the cone and can cause morphometric changes.

Thus, the major changes in the morphological parameters of present-day MAVF cones are the result of several factors: (1) weathering erosion, (2) gravity instability during volcanic activities, (3) vegetation, and (4) burial of the lava flow.

Some studies have shown that the morphometric parameters of the cones can highlight the geodynamic setting [42,43]. In the MAVF field, the average Hco/Wco value is very low (0.07) with a high Wcr/Wco value (0.47). Fornaciai et al. [43] proposed that cones associated in an extensional (intraplate) environment tend to have a lower average Hco/Wco (0.11 overall) than those associated with subduction and hotspots (0.15).

The analysis of geomorphological data of the Tabular Middle Atlas volcanoes was carried out to determine the maximum stresses (σHmax) at the time of emplacement. Consequently, the use of morphometric data of the cones offers the possibility to define the magma feeding system, and to reconstruct the tectonic evolution of the region [52]. Nakamura [51] reported that dikes propagate through the volcano, parallel to the maximum stresses (σHmax). Subsequently, Johnson and Harrison, and Strecker and Bosworth [53] used the alignment of volcanoes as a primary basis for deducing σHmax. In addition, Corazzato and Tibaldi, and Marliyan et al. [52,53] proposed that the alignment and elongation of craters, can indicate the orientation of tectonic stresses and the orientation of fractures, which feed volcanoes. In most cases, crater elongation parallels the subjacent magma-feeding fracture. However, the orientation of many breach bisectors appears to be incompatible with crater elongation, and the alignment of coeval cones due to several factors, such as faults, slope of pre-existing bedrock, or by deposition of volcanic material from recent and on-going eruptive activity. Among the examples that can be cited in this context are the H1 cone, the Boutjatiout cone (Figure 14a), and the Lachmine Izyar cone (Figure 13b).

On the other hand, we identified some aligned volcanoes, such as Hebri, H3, H2, H1, Habri, Mijmouane, and Tizi Idguel. The alignment of these volcanoes is relatively consistent with the elongation of the craters, and consistent with the orientation of regional tectonic stresses (Figure 14a). The alignment of three or more volcanic vents allows us to estimate the direction of the underlying fissure/dike, which constrains the direction of maximum horizontal stress (σHmax) at the time of fracture. Of these seven previous volcanoes, H2 and Tizi Idguel have a bisector azimuth of N345°, relatively parallel to the maximum stress (σHmax). The breaching of H1 was probably caused by a steeply sloping Habri volcano, favoring collapse in the ESE region of the cone (115°). This is because the slope of the pre-existing material can create morphological barriers that divert the direction of the breaching (Figure 14a).

Therefore, another alignment of the volcanoes is observed in accordance with the elongation of the craters of the volcanoes (Chtifat C1-C2 and C3, Chmil Assou, Lachmine

Izyar cone, and South Izyar). Both morphological parameters are also in relative accordance with the regional maximum stresses (σHmax). The breaching of the Lachmine Izyar cone was probably caused by a steep slope with high limestone bedrock, favoring collapse in the SE region of the cone (120°) (Figure 14b).

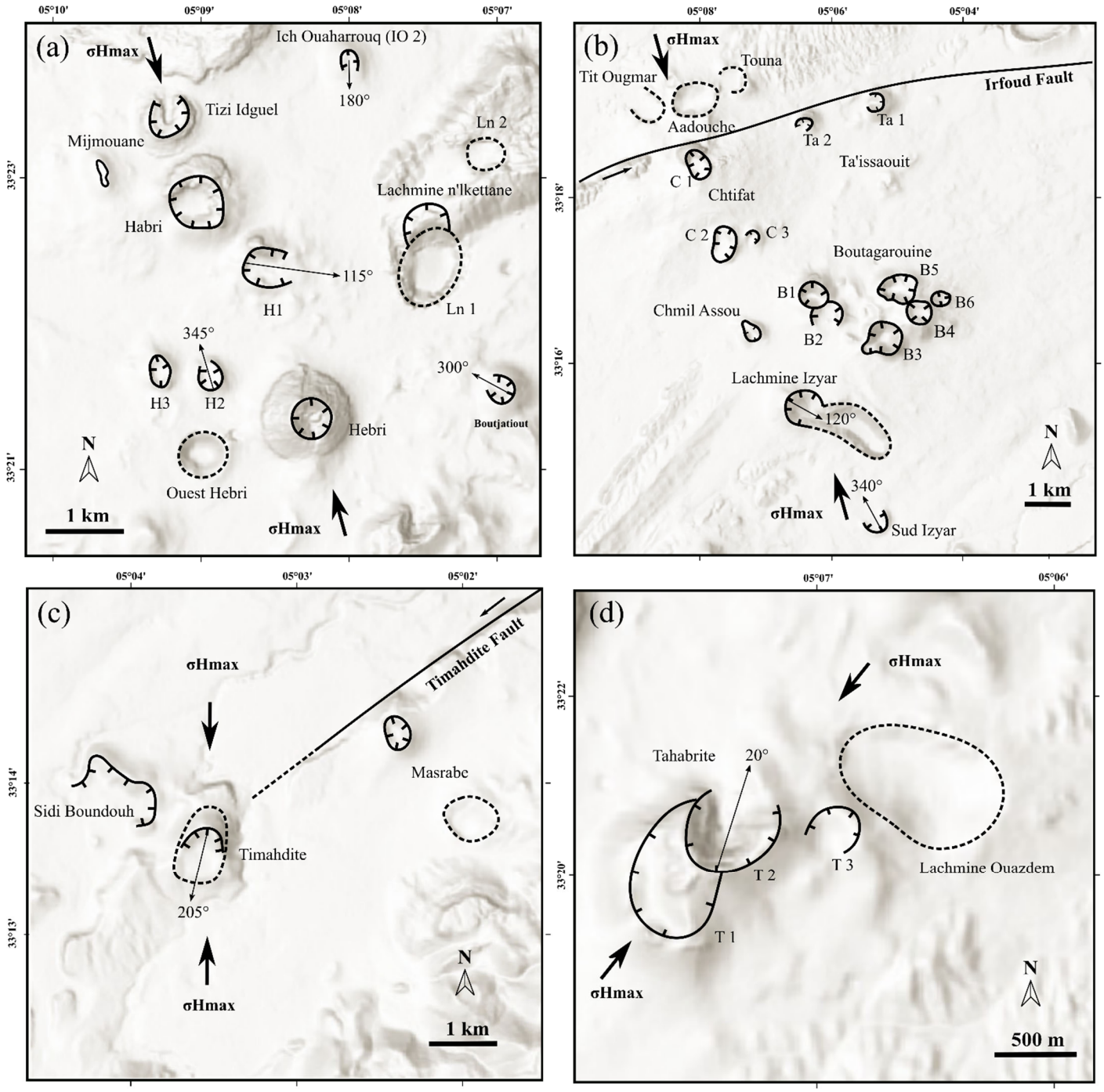

Figure 14. The distribution and alignment of volcanoes with the orientation of maximum horizontal stress (σHmax), the pointed circles correspond to maars, the circles correspond to scoria cones: (**a**) Hebri volcanic field; (**b**) Chtifat and Boutagarouine volcanic com-plex; (**c**) Timahdite volcanic field; (**d**) Tahabrite volcanic complex.

The Timahdite cone has an elongation of N230° and a breaching azimuth of N205°, due to the operation of the Timahdite sinister strike-slip fault. This has allowed the expression of a N-S-oriented fracture in which the Timahdite edifice is installed. This fracture is parallel to the maximum tectonic stress (N00°) (Figure 14c). This slight change

in stress is probably due to volcanic load. In the studies carried out, the volcanic load may be able to influence the structure of the strike-slip faults and the shear zone. This loading has locally modified the regional stress field, so that the extensional process starts at the cone, and the pre-existing faults become an extensional component [120,121].

The numerous examples observed, and the results obtained show that the volcanoes are part of a depressed zone between the Tizi n'Trettene Fault and the Middle North Atlasic Fault. This zone is bordered by normal faults with directions between N140° and N160°, and other existing faults with directions N20–40° and N40–50°, corresponding to the R and P fractures of the Riedel system in the sinistral strike-slip fault, respectively. The faults with directions N140° and N160°, where most of the volcanoes are located, are of type T. The major strike-slip faults have a N20-N40° to N40–50° veering. The N40–50° direction is also the direction of several volcanic alignments, such as the Tahabrite volcanic complex (Figure 14d).

For the maars, most of the monogenetic volcanoes are observed grouped in the Larouche area, and are isolated from the strombolian cones (e.g., Boubalghattene complex, N'Ait Lhaj complex). There is another grouping of three maars in the Touna area (Touna maar, Tit Ougmar and Aadouche) and a grouping of two maars in the south-western part of Timahdite (Lachmine Lakbir and Sghir). Although not all the maars have an elongation orientation corresponding to a mode, these data reveal a commonality with some volcanoes in the literature, such as the Lamongan volcanic field in Indonesia [122] and the Pinacate volcanic field in Mexico [123,124].

Converging maars or maars located in the same lineament do not show similar elongation, suggesting that regional stresses influencing dyke propagation do not strongly control elongation of the volcano itself, as also described in the work of Nichols and Graettinger [87]. The MAVF maar lineaments do not have a similar orientation to the cone lineaments, and do not match the trend of the main regional fault (NE-SW). The evolution of conceptual models of maar formation, based on recent field research, proposes that sill formation, and dynamic stress regimes generated by the eruption itself, should be considered as localized variations in hydrology and rock resistance, and as influences on the lateral migration of explosion sites during a maar-forming eruption [85,125].

From our persepctive, the volcanic complexes of Boubalghattene, Touna, and Lachmine n'Ait Lhaj in the Larouche region are probably controlled by the reactivation of the Irfoud inherited fault (N70°) and the Loubatène-Chtifat fault (N70°). In the Middle Quaternary, the Timahdite fault is probably responsible for the emplacement of the Timahdite maar with its cone at the top via a submeridian fracture. An NE-SW-oriented fault corridor can be observed, which is probably responsible for the emplacement of Lachmine N'kettane (Ln1, 2) and Michlifene.

The geological interest of this volcanic province is based on the presence of numerous volcanoes of very varied forms, namely maars, unbreached or breached scoria cones, as well as composite edifices. These phreatomagmatic and volcanic apparatuses produced very diverse pyroclastic products (e.g., ashes, bombs, lapilli, pumice), as well as lava flows of varied morphologies (transition of pāhohoe- 'aā, clastogenic dyke, etc.). The transition of lava is remarkable on some sites. Pāhoehoe lava can evolve into 'aā, reflecting temperature drop, and crystallization-enhanced viscosity increases, slowing the flow movement and making the surface broken and contorted [104,126–128] [96,98–101]. Obviously, magma composition is a determining factor for the type of flow that is formed in relation to other factors, such as temperature, crystal content, lava deformation (shear rate), crystallinity, and volatile content/vesicularity; along with external influences, such as the mechanism of emission, the rate of effusion, the flow velocity, the topography, and the slope failure [129]. As far as the slope is concerned, slope failure can cause the pāhohoe-'aā transition due to the acceleration of the lava at constant temperature. Sometimes the transition can also be made by a simple decrease in temperature, and therefore, an increase in viscosity during the advance of the flow. In this study, perhaps this rapid transition is the result of a high viscosity of the lava, or by a very low deformation rate. This type of

transition is very common in basaltic volcanic provinces, and many examples of this rapid transition as a function of viscosity and deformation rate have been documented in the literature, among others; e.g. in the Kilauea volcano, Hawaii [106]. The observations of Peterson and Tilling [104] show that there is a critical correlation between viscosity and shear deformation rates.

In parallel to the existence of various structures of the Middle Atlas, such as hornitos, tumuli, and the basalt organ outcropping, we witness the emergence of other structures, such as clastogenic dyke structures, in the volcano Aguelmam Sidi Ali. In the literature, these structures of lavas dyke have been interpreted as squeeze-up intrusions, formed during the formation of the clastogenic lava flow during the eruption fissures and the collapse of scoria cones [130]. These dykes sometimes exhibit eutaxial texture, with the presence of highly deformed pyroclasts, like those observed in the spatter deposits. Where these intrusions are directly fed from below by clastogenic lavas, they are considered clastogenic dykes [131]. In contrast, the clastogenic deposits of Timahdite volcano are inferred to be primarily formed by the lava fountain [30].

These different morphological and geological characteristics make the volcanic province of the Middle Atlas a true exceptional geosite with heritage value that deserves to be recognized so that it can be protected to meet the needs of the field [8].

The great geographical concentration of these volcanoes and the diversity of their products offer opportunities for the development of geotourism and constitute a real educational field for all categories of visitors (scientific and educational interests par excellence, but also recreational, cultural, geotouristic, and economic interests, and in the framework of sustainable development).

6. Conclusion

The mafic volcanism considered covers an area of 1500 km^2 with a total volume of solid material estimated at more than 80 km^3 and is the basis for the formation of 87 monogenic volcanoes distinguished by effusive activity and mixed activity, such as scoria cones from explosive eruptions of strombolian type and hydrovolcanic explosive eruptions creating tuff rings and maars. These types of monogenic volcanoes have been distinguished according to their topographic, geological, geomorphological, structural, and volcanic evolution. The eruptive material of these events affects most of the Middle Atlas, and consists of pyroclastic fallout, pyroclastic density stream deposits, and widespread nephelinite, basanitic, and alkaline/subalkaline lava flows with diverse surface textures (Pāhoehoe, aa, clastogenic).

Of the 44 scoria cones identified, 23 scoria cones were unbreached and 21 were breached. These cones exhibit a wide range of aspect ratios (AR) and elongation (El), of which 11% of the cones are equant. The other scoria cones represent elongated and sometimes composite crater shapes. The mean Hco/Wco ratio of the breached cones is also the same value as that of the unbreached cones. This value is close to the average value for the Chubut volcanic field in Argentina (Hco/Wco = 0.08), and in very low correlation with the values of Settle and Porter [35,85]. This means that part of the MAVF cones is usually characterized by multiple vents or superimposed structures, generating a larger basal extent relative to Hco. This low ratio of most MAVF scoria cones is a consequence of scoria cone degradation by weathering and gravity instability over time, resulting in increased basal cone diameter and decreased cone height, as well as reduced slopes. From the last glacial period (25,000 cal. BP) to the present, the degradation of the scoria cones by the above processes is very low due to the presence of intense vegetation at that time.

In the MAVF, there are 24 recognized maars, and 15 maars have an open crater. Five maars have a closed crater. A total of 64% of the maars have a semi-elliptical to semicircular morphology and the rest oscillate between a regular, elliptic, or composite shape. The maars of the MAVF are located on a limestone base of Liassic and Eocene age. The main parameter influencing the size of the craters and the variation of the shape of the Middle Atlas maars is the distribution and physical state of the water in these limestones.

Thus, field observations reveal many cases of phreatomagmatic to magmatic transition and vice versa, resulting from the variation and depletion of the water source, such as Timahdite (maar-cone), Lechmine Lakbir (maar-cone), Lechmine N'kettane (Ln1) (maar-cone), and West of Hebri (maar-cone). The low Hco/Wco ratio and the large increase in Wcr/Wco ratio of the maars compared to the scoria cones result from the growth mode of the system during the eruption, i.e., the maars have a crater diameter value relatively close to that of the maar cone, and the height is also very low compared to the crater diameter and the maar cone.

Most of the volcanoes are aligned in a direction consistent with the orientation of regional tectonic stresses (N140–160°) over a length of 70 km. The N20–N40° direction and N40–50° direction are also the direction of several volcanic alignments, such as the Tahabrite volcanic complex. In contrast to the scoria cone, the Middle Atlas maars have a set of closely spaced craters aligned parallel to the strike-slip faults (N70°).

Author Contributions: Conceptualization, M.B. and K.N.; methodology, M.B. and K.N.; software, M.B.; validation, M.B., M.J. and E.H.T.; formal analysis, M.B.; investigation, M.B. M.J. and E.H.T.; resources, M.B.; data curation, M.B.; writing—original draft preparation, M.B.; writing—review and editing, K.N., M.J. and E.H.T.; visualization, M.B.; supervision, K.N. and E.H.T.; project administration, M.B.; funding acquisition, M.B. All authors have read and agreed to the published version of the manuscript.

Funding: Please add: This research received no external funding.

Institutional Review Board Statement: Not applicable.

Informed Consent Statement: Not applicable.

Data Availability Statement: Not applicable.

Acknowledgments: We thank the inhabitants of the region of Azrou for their help and their kindness. We thank the anonymous reviewers for their constructive comments on the manuscript.

Conflicts of Interest: The authors declare no conflict of interest.

References

1. Németh, K.; Kereszturi, G. Monogenetic volcanism: Personal views and discussion. *Int. J. Earth Sci.* **2015**, *104*, 2131–2146. https://doi.org/10.1007/s00531-015-1243-6.
2. Wood, C.A. Morphometric analysis of cinder-cone degradation. *J. Volcanol. Geotherm. Res.* **1980**, *8*, 137–160.
3. Connor, C.B.; Conway, F.M. Basaltic volcanic fields. In *Encyclopedia of Volcanoes*; Sigurdsson, H., Ed.; Academic Press: San Diego, CA, USA, 2000; pp. 331–343.
4. Chorowicz, J. The East African rift system. *J. Afr. Earth Sci.* **2005**, *43*, 379–410. https://doi.org/10.1016/j.jafrearsci.2005.07.019.
5. Rapprich, V.; Cajz, V.; Kostak, M.; Pecskay, Z.; Ridkosil, T.; Raska, P.; Radon, M. Reconstruction of eroded monogenic Strombolian cones of Miocene age: A case study on character of volcanic activity of the Jicin Volcanic Field (NE Bohemia) and subsequent erosional rates estimation. *J. GEOSCI* **2007**, *52*, 169–180.
6. Valentine, G.A.; Gregg, T.K.P. Continental basaltic volcanoes—Processes and problems. *J. Volcanol. Geotherm. Res.* **2008**, *177*, 857–873. https://doi.org/10.1016/j.jvolgeores.2008.01.050.
7. Németh, K.; Casadevall, T.; Moufti, M.R.; Marti, J. Volcanic Geoheritage. *Geoheritage* **2017**, *9*, 251–254. https://doi.org/10.1007/s12371-017-0257-9.
8. Baadi, K.; Amine, A.; Zangmo Tefogoum, G.; Sabaoui, A.; Tekiout, B. Volcanic geosites assessment in the Plio-Quaternary Azrou-Timahdite Plateau (Middle Atlas, Morocco). *J. Afr. Earth Sci.* **2021**, *184*, 104352. https://doi.org/10.1016/j.jafrearsci.2021.104352.
9. Zangmo, G.T.; Kagou, A.D.; Nkouathio, D.G.; Gountie, M.D.; Kamgang, P. The Volcanic Geoheritage of the Mount Bamenda Calderas (Cameroon Line): Assessment for Geotouristic and Geoeducational Purposes. *Geoheritage* **2017**, *9*, 255–278. https://doi.org/10.1007/s12371-016-0177-0.
10. Erfurt-Cooper, P. Ed. *Volcanic Tourist Destinations*. Springer: Berlin/Heidelberg, Germany, 2014; p. 384.
11. Erfurt-Cooper, P. Geotourism in volcanic and geothermal environments: Playing with fire? *Geoheritage* **2011**, *3*, 187–193. https://doi.org/10.1007/s12371-010-0025-6.
12. Joyce, B. Volcano tourism in the new Kanawinka Global Geopark of Victoria and SE South Australia. In *Volcano and Geothermal Tourism, Sustainable Geo-Resources for Leisure and Recreation*; Erfurt-Cooper, P., Cooper, M., Eds.; Earthscan: London, UK, 2010; pp. 302–311.

13. Ertekin, C.; Ekinci, Y.L.; Buyuksarac, A.; Ekinci, R. Geoheritage in a Mythical and Volcanic Terrain: An Inventory and Assessment Study for Geopark and Geotourism, Nemrut Volcano (Bitlis, Eastern Turkey). *Geoheritage* **2021**, *13*, 73. https://doi.org/10.1007/s12371-021-00593-5.
14. Guilbaud, M.-N.; del Pilar Ortega-Larrocea, M.; Cram, S.; de Vries, B.v.W. Xitle Volcano Geoheritage, Mexico City: Raising Awareness of Natural Hazards and Environmental Sustainability in Active Volcanic Areas. *Geoheritage* **2021**, *13*, 6. https://doi.org/10.1007/s12371-020-00525-9.
15. Galas, A.; Paulo, A.; Gaidzik, K.; Zavala, B.; Kalicki, T.; Churata, D.; Galas, S.; Marino, J. Geosites and Geotouristic Attractions Proposed for the Project Geopark Colca and Volcanoes of Andagua, Peru. *Geoheritage* **2018**, *10*, 707–729. https://doi.org/10.1007/s12371-018-0307-y.
16. Migon, P.; Pijet-Migon, E. Overlooked geomorphological component of volcanic geoheritage-diversity and perspectives for tourism industry, Pogrze Kaczawskie Region, SW Poland. *Geoheritage* **2016**, *8*, 333–350. https://doi.org/10.1007/s12371-015-0166-8.
17. Rapprich, V.; Lisec, M.; Fiferna, P.; Zavada, P. Application of Modern Technologies in Popularization of the Czech Volcanic Geoheritage. *Geoheritage* **2017**, *9*, 413–420. https://doi.org/10.1007/s12371-016-0208-x.
18. Khalaf, E.; Wahed, M.A.; Maged, A.; Mokhtar, H. Volcanic Geosites and Their Geoheritage Values Preserved in Monogenetic Neogene Volcanic Field, Bahariya Depression, Western Desert, Egypt: Implication for Climatic Change-Controlling Volcanic Eruption. *Geoheritage* **2019**, *11*, 855–873. https://doi.org/10.1007/s12371-018-0336-6.
19. Kil, Y.; Ahn, K.S.; Woo, K.S.; Lee, K.C.; Jwa, Y.-J.; Jung, W.; Sohn, Y.K. Geoheritage Values of the Quaternary Hantangang River Volcanic Field in the Central Korean Peninsula. *Geoheritage* **2019**, *11*, 765–782. https://doi.org/10.1007/s12371-018-0329-5.
20. El Azzouzi, M.; Maury, R.C.; Bellon, H.; Youbi, N.; Cotten, J.; Kharbouch, F. Petrology and K-Ar chronology of the Neogene-Quaternary Middle Atlas basaltic province, Morocco. *Bulletin Société Géologique France* **2010**, *181*, 243–257.
21. Blache, J. Termier (Henri).—Etudes géologiques sur le Maroc central et le Moyen-Atlas septentrional. *Revue Géographie Alpine* **1937**, *25*, 525–529.
22. Moukadiri, A.; Kornprobst, J. *Garnet and/or Spinel Bearing Pyroxenites in Alkali Basalts Near Azrou (Middle Atlas, Morocco): Mantle Derived Alumina-Rich Xenoliths Related to the "Ariegite-Grospydite" Trend*; Elsevier: Amsterdam, The Netherlands, 1984.
23. Harmand, C.; Moukadiri, A. Synchronisme entre tectonique compressive et volcanisme alcalin; exemple de la province quaternaire du Moyen Atlas (Maroc). *Bulletin Société Géologique France* **1986**, *II*, 595-603. https://doi.org/10.2113/gssgfbull.II.4.595.
24. Moukadiri, A.; Pin, C. Géochimie/Geochemistry Géomatériaux / Geomaterials Géochimie (éléments majeurs et terres rares) des granulites méta-sédimentaires en xénolithes dans les basaltes alcalins quaternaires du Moyen Atlas (Maroc): Arguments en faveur de la nature pour partie restitique de la croûte inférieure. *Comptes Rendus de l'Académie des Sciences—Series IIA—Earth and Planetary Science* **1998**, *327*, 589–595. https://doi.org/10.1016/S1251-8050(99)80112-8.
25. Natali, C.; Beccaluva, L.; Bianchini, G.; Ellam, R.M.; Siena, F.; Stuart, F.M. Carbonated alkali-silicate metasomatism in the North Africa lithosphere: Evidence from Middle Atlas spinel-lherzolites, Morocco. *J. South Am. Earth Sci.* **2013**, *41*, 113–121.
26. El Messbahi, H.; Bodinier, J.-L.; Vauchez, A.; Dautria, J.-M.; Ouali, H.; Garrido, C.J. Short wavelength lateral variability of lithospheric mantle beneath the Middle Atlas (Morocco) as recorded by mantle xenoliths. *Tectonophysics* **2015**, *650*, 34–52. https://doi.org/10.1016/j.tecto.2014.11.020.
27. Chanouan, L.; Ikenne, M.; Gahlan, H.A.; Arai, S.; Youbi, N. Petrological characteristics of mantle xenoliths from the Azrou-Timahdite quaternary basalts, middle atlas, Morocco: A mineral chemistry perspective. *J. Afr. Earth Sci.* **2017**, *127*, 235–252. https://doi.org/10.1016/j.jafrearsci.2016.09.004.
28. Bosch, D.; Maury, R.C.; El Azzouzi, M.h.; Bollinger, C.; Bellon, H.; Verdoux, P. Lithospheric origin for Neogene–Quaternary Middle Atlas lavas (Morocco): Clues from trace elements and Sr–Nd–Pb–Hf isotopes. *Lithos* **2014**, *205*, 247–265. https://doi.org/10.1016/j.lithos.2014.07.009.
29. Lakroud, K.; Remmal, T.; El Amrani, I.; Mountaj, S.; El Kamel, F.; Van Wyk de Vries, B.; Boivin, P.; Balcone-Boissard, H.; Makhoukhi, Soufi, M. Monogenetic Strombolian Activity at Aguelmane Sidi Ali Volcano (Middle Atlas Volcanic Province, Morocco). *Geogr. Bull.* **2019**, *60*, 109–125.
30. Benamrane, M.; Jadid, M.; Dahmani, H.; Talbi, F. The eruptive history of the Timahdite monogeneteic Quaternary volcano (Middle Atlas, Morocco). *Quaternaire* **2020**, *31*, 309–326.
31. Amine, A.; Hassani, I.-E.E.A.E.; Remmal, T.; Kamel, F.E.; Vries, B.V.W.D.; Boivin, P. Geomorphological Classification and Landforms Inventory of the Middle-Atlas Volcanic Province (Morocco): Scientific Value and Educational Potential. *Quaest. Geogr.* **2019**, *38*, 107–129. https://doi.org/10.2478/quageo-2019-0010.
32. Mountaj, S.; Mhiyaoui, H.; Remmal, T.; Makhoukhi, S.; Kamel, F.E. Study of Monogenic Volcanism in a Karstic System: Case of the Maar of Lechmine n'Aït el Haj (Middle Atlas, Morocco). In *Updates in Volcanology—Transdisciplinary Nature of Volcano Science*; Németh, K., Ed.; IntechOpen: Rijeka, London, UK, 2020; pp. 1–24. https://doi.org/10.5772/intechopen.94756.
33. Mountaj, S.; Remmal, T.; El Amrani, I.E.E.; Makhoukhi, S.; Lakroud, K.; de Vries, B.V. Phreatomagmatic plioquaternary volcanism in the Middle Atlas: Analysis of the eruptive sequence of the Lechmine n'Ait El Haj maar. *Arab. J. Geosci.* **2020**, *13*, 559. https://doi.org/10.1007/s12517-020-05554-w.
34. Mountaj, S.; Toufik, R.; Lakroud, K.; Boivin, P.; el Amrani, I.-e.E.H.; El Kamel, F.; Makhoukhi, S.; Jounaid, H.; Amraoui, F.; Soufi, M. The Volcanic Field of the Middle Atlas Causse: Highlights and Heritage Appropriation. *Geogr. Bull.* **2019**, *60*, 127–147.

35. Scott, D.H.; Trask, N.J. Geology of the Lunar Crater volcanic field, Nye County, Nevada. *U.S. Geol. Surv. Prof. Paper* **1971**, *599-I*, 1-22.
36. Settle, M. Structure and Emplacement of Cinder Cone Fields. *Am. J. Sci.* **1979**, *279*, 1089–1107.
37. Hooper, D.M.; Sheridan, M.F. Computer-simulation models of scoria cone degradation. *J. Volcanol. Geotherm. Res.* **1998**, *83*, 241–267.
38. Inbar, M.; Risso, C. A morphological and morphometric analysis of a high density cinder cone volcanic field—Payun Matru, south-central Andes, Argentina. *Zeitschrift für Geomorphologie* **2001**, *45*, 321–343.
39. Grosse, P.; de Vries, B.V.; Euillades, P.A.; Kervyn, M.; Petrinovic, I.A. Systematic morphometric characterization of volcanic edifices using digital elevation models. *Geomorphology* **2012**, *136*, 114–131. https://doi.org/10.1016/j.geomorph.2011.06.001.
40. Bemis, K.; Walker, J.; Borgia, A.; Turrin, B.; Neri, M.; Swisher, C., III. The growth and erosion of cinder cones in Guatemala and El Salvador; models and statistics. *J. Volcanol. Geotherm. Res.* **2011**, *201*, 39–52. http://dx.doi.org/10.1016/j.jvolgeores.2010.11.007.
41. Kereszturi, G.; Németh, K. Post-eruptive sediment transport and surface processes on unvegetated volcanic hillslopes—A case study of Black Tank scoria cone, Cima Volcanic Field, California. *Geomorphology* **2016**, *267*, 59–75. https://doi.org/10.1016/j.geomorph.2016.05.023.
42. Tibaldi, A. Morphology of pyroclastic cones and tectonics. *J. Geophys. Res. -Solid Earth* **1995**, *100*, 24521–24535.
43. Fornaciai, A.; Favalli, M.; Karatson, D.; Tarquini, S.; Boschi, E. Morphometry of scoria cones, and their relation to geodynamic setting; a DEM-based analysis. *J. Volcanol. Geotherm. Res.* **2012**, *217–218*, 56–72. http://dx.doi.org/10.1016/j.jvolgeores.2011.12.012.
44. Uslular, G.; Le Corvec, N.; Mazzarini, F.; Legrand, D.; Gencalioglu-Kuscu, G. Morphological and multivariate statistical analysis of quaternary monogenetic vents in the Central Anatolian Volcanic Province (Turkey): Implications for the volcano-tectonic evolution. *J. Volcanol. Geotherm. Res.* **2021**, *416*, 107280. https://doi.org/10.1016/j.jvolgeores.2021.107280.
45. Favalli, M.; Karatson, D.; Mazzarini, F.; Pareschi, M.T.; Boschi, E. Morphometry of scoria cones located on a volcano flank: A case study from Mt. Etna (Italy), based on high-resolution LiDAR data. *J. Volcanol. Geotherm. Res.* **2009**, *186*, 320–330. https://doi.org/10.1016/j.jvolgeores.2009.07.011.
46. Bemis, K.; Ferencz, M. Morphometric analysis of scoria cones: The potential for inferring process from shape. In *Monogenetic Volcanism*; Németh, K., Carrasco-Nuñez, G., Aranda-Gomez, J.J., Smith, I.E.M., Eds.; The Geological Society Publishing House: Bath, UK, 2017; Volume 446.
47. Kereszturi, G.; Jordan, G.; Németh, K.; Doniz-Paez, J.F. Syn-eruptive morphometric variability of monogenetic scoria cones. *Bull. Volcanol.* **2012**, *74*, 2171–2185. https://doi.org/10.1007/s00445-012-0658-1.
48. Kereszturi, G.; Németh, K. Structural and morphometric irregularities of eroded Pliocene scoria cones at the Bakony-Balaton Highland Volcanic Field, Hungary. *Geomorphology* **2012**, *136*, 45–58.
49. Doniz, J.; Romero, C.; Coello, E.; Guillen, C.; Sanchez, N.; Garcia-Cacho, L.; Garcia, A. Morphological and statistical characterisation of recent mafic volcanism on Tenerife (Canary Islands, Spain). *J. Volcanol. Geotherm. Res.* **2008**, *173*, 185–195. https://doi.org/10.1016/j.jvolgeores.2007.12.046.
50. Baez, W.; Carrasco-Nunez, G.; Giordano, G.; Viramonte, J.G.; Chiodi, A. Polycyclic scoria cones of the Antofagasta de la Sierra Basin, southern Puna plateau, Argentina. *Spec. Publ. Geol. Soc. Lond.* **2016**, *446*, 311. http://dx.doi.org/10.1144/SP446.3.
51. Nakamura, K. Volcanoes as possible indicators of tectonic stress orientation- principal and proposal. *J. Volcanol. Geotherm. Res.* **1977**, *2*, 1–16.
52. Corazzato, C.; Tibaldi, A. Fracture control on type, morphology and distribution of parasitic volcanic cones: An example from Mt. Etna, Italy. *J. Volcanol. Geotherm. Res.* **2006**, *158*, 177–194.
53. Marliyani, G.I.; Helmi, H.; Arrowsmith, J.R.; Clarke, A. Volcano morphology as an indicator of stress orientation in the Java Volcanic Arc, Indonesia. *J. Volcanol. Geotherm. Res.* **2020**, *400*, 106912. https://doi.org/10.1016/j.jvolgeores.2020.106912.
54. Missenard, Y.; Zeyen, H.; Frizon de Lamotte, D.; Leturmy, P.; Petit, C.; Sébrier, M.; Saddiqi, O. Crustal versus asthenospheric origin of relief of the Atlas Mountains of Morocco. *J. Geophys. Res. Solid Earth* **2006**, *111*. https://doi.org/10.1029/2005JB003708.
55. de Lamotte, D.F.; Leturmy, P.; Missenard, Y.; Khomsi, S.; Ruiz, G.; Saddiqi, O.; Guillocheau, F.; Michard, A. Mesozoic and Cenozoic vertical movements in the Atlas system (Algeria, Morocco, Tunisia): An overview. *Tectonophysics* **2009**, *475*, 9–28. https://doi.org/10.1016/j.tecto.2008.10.024.
56. Fedan, B. Evolution Géodynamique d'un Bassin Intra-Plaque Sur Décrochement: Le Moyen Atlas Durant Le Méso-Cénozoïque. *Trav. Inst. Sci. Rabat.* **1988**, *18*, 142.
57. Froitzheim, N.; Stets, J.; Wurster, P. Aspects of Western High Atlas Tectonics. In *The Atlas System of Morocco*; Jacobshagen, V.H., Ed.; Springer-Verlag: Berlin/Heidelberg, Germany, 1988; Volume Lecture Notes in Earth Sciences, pp. 219–244.
58. Choubert, G.; Marcais, J. *Aperçu Structural in Géologie Du Maroc*; XIXéme Congés Géol. Inten.: Alger, Algiers, 1952; Volume 3ème série, Maroc, n° 6, 2 cartes, Notes et Mém. Serv. Géol., Maroc, pp. 9–73.
59. Charriere, A. Evolution neogene de bassins continentaux et marins dans le Moyen Atlas central (Maroc). *Bulletin Société Géologique France* **1984**, *S7-XXVI*, 1127–1136. https://doi.org/10.2113/gssgfbull.S7-XXVI.6.1127.
60. Choubert, G. Carte Géologique Du Maroc Au 1/500 000, Feuille de Rabat. *Notes Mém. Serv. Géol. Maroc* **1956**, *70*.
61. Hollard, H.; Choubert, G.; Bronner, G.; Marchand, J.; Sougy, J. Carte Géologique Du Maroc, Scale 1: 1,000,000. *Serv. Carte géol. Maroc* **1985**, *260*.

62. Amraoui, F. *Contribution à La Reconnaissance Des Aquifères Karstique, Cas Du Lias de La Plaine de Sais et Du Causse Moyen Atlasique Tabulaire (Maroc)*; Hassan ii Ain Chock University: Casablanca, Morocco, 2005.
63. Herbig, H.-G. Synsedimentary Tectonics in the Northern Middle Atlas (Morocco) during the Late Cretaceous and Tertiary. In *The Atlas System of Morocco*; Jacobshagen, V.H., Ed.; Springer: Berlin/Heidelberg, Germany, 1988; Volume 15, pp. 321–337.
64. Charrière, A. Héritage Hercynien et Évolution Géodynamique Alpine d'une Chaine Intracontinentale : Le Moyen-Atlas Au Sud-Est de Fes (Maroc). 1990.
65. Ait Brahim, L.; Chotin, P.; Hinaj, S.; Abdelouafi, A.; El Adraoui, A.; Nakcha, C.; Dhont, D.; Charroud, M.; Sossey Alaoui, F.; Amrhar, M.; et al. Paleostress evolution in the Moroccan African margin from Triassic to Present. *Tectonophysics* **2002**, *357*, 187–205. https://doi.org/10.1016/S0040-1951(02)00368-2.
66. Morel, J.L.; Zouine, M.; Poisson, A. Relations entre la subsidence des bassins moulouyens et la creation des reliefs atlasiques (Maroc); un exemple d'inversion tectonique depuis le Neogene. *Bulletin Société Géologique France* **1993**, *164*, 79–91.
67. Petit, J.P.; Raynaud, S.; Cautru, J.P. Microtectonique cassante lors du plissement d'un conglomerat (Mio-Pliocene du Haut Atlas; Maroc). *Bulletin Société Géologique France* **1985**, *I*, 415–421. https://doi.org/10.2113/gssgfbull.I.3.415.
68. Chardon, M. Martin (J.).—Le Moyen Atlas Central. Etude géomorphologique. *Revue Géographie Alpine* **1982**, *70*, 444.
69. Lowell, J.D. Mechanics of basin inversion from worldwide examples. *Geol. Soc. Lond. Spec. Publ.* **1995**, *88*, 39–57. https://doi.org/10.1144/GSL.SP.1995.088.01.04.
70. Outtani, F.; Addoum, B.; Mercier, E.; de Lamotte, D.F.; Andrieux, J. Geometry and kinematics of the South Atlas Front, Algeria and Tunisia. *Tectonophysics* **1995**, *249*, 233–248. https://doi.org/10.1016/0040-1951(95)00022-F.
71. Thomas, G.; Fedan, B. Découverte de dépôts néogènes déformés par l'accident nord-moyen atlasique (Maroc). Implications sur son activité mio-plio-quaternaire au Nord de Boulemane. *Géologie Méditerranéenne* **1985**, *12*, 151–154.
72. Ayarza, P.; Alvarez-Lobato, F.; Teixell, A.; Arboleya, M.L.; Tesón, E.; Julivert, M.; Charroud, M. Crustal structure under the central High Atlas Mountains (Morocco) from geological and gravity data. *Tectonophysics* **2005**, *400*, 67–84. https://doi.org/10.1016/j.tecto.2005.02.009.
73. Teixell, A.; Ayarza, P.; Zeyen, H.; Fernàndez, M.; Arboleya, M.-L. Effects of mantle upwelling in a compressional setting: The Atlas Mountains of Morocco. *Terra Nova* **2005**, *17*, 456–461. https://doi.org/10.1111/j.1365-3121.2005.00633.x.
74. Fullea, J.; Fernàndez, M.; Afonso, J.C.; Vergés, J.; Zeyen, H. The structure and evolution of the lithosphere–asthenosphere boundary beneath the Atlantic–Mediterranean Transition Region. *Lithos* **2010**, *120*, 74–95. https://doi.org/10.1016/j.lithos.2010.03.003.
75. Bezada, M.J.; Humphreys, E.D.; Davila, J.M.; Carbonell, R.; Harnafi, M.; Palomeras, I.; Levander, A. Piecewise delamination of Moroccan lithosphere from beneath the Atlas Mountains. *Geochem. Geophys. Geosyst.* **2014**, *15*, 975–985. https://doi.org/10.1002/2013GC005059.
76. Miller, M.S.; Becker, T.W. Reactivated lithospheric-scale discontinuities localize dynamic uplift of the Moroccan Atlas Mountains. *Geology* **2014**, *42*, 35–38. https://doi.org/10.1130/g34959.1.
77. Palomeras, I.; Thurner, S.; Levander, A.; Liu, K.; Villasenor, A.; Carbonell, R.; Harnafi, M. Finite-frequency Rayleigh wave tomography of the western Mediterranean: Mapping its lithospheric structure. *Geochem. Geophys. Geosyst.* **2014**, *15*, 140–160. https://doi.org/10.1002/2013GC004861.
78. Duggen, S.; Hoernle, K.A.; Hauff, F.; Klügel, A.; Bouabdellah, M.; Thirlwall, M.F. Flow of Canary mantle plume material through a subcontinental lithospheric corridor beneath Africa to the Mediterranean. *Geology* **2009**, *37*, 283–286. https://doi.org/10.1130/g25426a.1.
79. Missenard, Y.; Cadoux, A. Can Moroccan Atlas lithospheric thinning and volcanism be induced by Edge-Driven Convection? *Terra Nova* **2012**, *24*, 27–33. https://doi.org/10.1111/j.1365-3121.2011.01033.x.
80. Fullea Urchulutegui, J.; Fernàndez, M.; Zeyen, H. Lithospheric structure in the Atlantic–Mediterranean transition zone (southern Spain, northern Morocco): A simple approach from regional elevation and geoid data. *Comptes Rendus Geosci.* **2006**, *338*, 140–151. https://doi.org/10.1016/j.crte.2005.11.004.
81. Termier, H.; Termier, G.; Jouravsky, G. Une Roche Volcanique à Gros Grain de La Famille Des Ijolites: La Talzastite. *Notes du Service Géologique du Maroc* **1948**, *1*, 81–120.
82. Harmand, C.; Cantagrel, J.M. Le volcanisme alcalin tertiaire et quaternaire du moyen atlas (Maroc): Chronologie K/Ar et cadre géodynamique. *J. Afr. Earth Sci.* **1984**, *2*, 51–55. https://doi.org/10.1016/0899-5362(84)90019-8.
83. Doniz-Paez, J.; Romero-Ruiz, C.; Sanchez, N. Quantitative size classification of scoria cones: The case of Tenerife (Canary Islands, Spain). *Phys. Geogr.* **2012**, *33*, 514–535. https://doi.org/10.2747/0272-3646.33.6.514.
84. Hasenaka, T.; Carmichael, I.S.E. A compilation of location, size, and geomorphological parameters of volcanoes of the Michoacan-Guanajuato volcanic field, central Mexico. *Geofis. Int.* **1985**, *24*, 577–608. https://doi.org/10.22201/igeof.00167169p.1985.24.4.2179
85. Graettinger, A.H. Trends in maar crater size and shape using the global Maar Volcano Location and Shape (MaarVLS) database. *J. Volcanol. Geotherm. Res.* **2018**, *357*, 1–13. https://doi.org/10.1016/j.jvolgeores.2018.04.002.
86. Paulsen, T.S.; Wilson, T.J. New criteria for systematic mapping and reliability assessment of monogenetic volcanic vent alignments and elongate volcanic vents for crustal stress analyses. *Tectonophysics* **2010**, *482*, 16–28. https://doi.org/10.1016/j.tecto.2009.08.025.

87. Nichols, C.; Graettinger, A. The influence of regional stress and structural control on the shape of maar craters. *Volcanica* **2021**, *4*, 23–39. https://doi.org/10.30909/vol.04.01.2339.
88. Moufti, M.R.; Németh, K.; Murcia, H.; Lindsay, J.M.; El-Masry, N. Geosite of a steep lava spatter cone of the 1256 AD, Al Madinah eruption, Kingdom of Saudi Arabia. *Cent. Eur. J. Geosci.* **2013**, *5*, 189–195. https://doi.org/10.2478/s13533-012-0123-x.
89. Seib, N.; Kley, J.; Buchel, G. Identification of maars and similar volcanic landforms in the West Eifel Volcanic Field through image processing of DTM data: Efficiency of different methods depending on preservation state. *Int. J. Earth Sci.* **2013**, *102*, 875–901. https://doi.org/10.1007/s00531-012-0829-5.
90. Németh, B.; Németh, K.; Procter, J.N. Visitation Rate Analysis of Geoheritage Features from Earth Science Education Perspective Using Automated Landform Classification and Crowdsourcing: A Geoeducation Capacity Map of the Auckland Volcanic Field, New Zealand. *Geosciences* **2021**, *11*, 480. https://doi.org/10.3390/geosciences11110480.
91. Porter, S.C. Distribution, morphology, and size frequency of cinder cones on Mauna Kea Volcano, Hawaii. *Geol. Soc. Am. Bull.* **1972**, *83*, 3613–3626. https://doi.org/10.1130/0016-7606(1972)83[3607:DMASFO]2.0.CO;2
92. Sato, H.; Taniguchi, H. Relationship between crater size and ejecta volume of recent magmatic and phreato-magmatic eruptions: Implications for energy partitioning. *Geophys. Res. Lett.* **1997**, *24*, 205–208. https://doi.org/10.1029/96GL04004
93. Gevrek, A.I.; Kazanci, N. A Pleistocene, pyroclastic-poor maar from central Anatolia, Turkey: Influence of a local fault on a phreatomagmatic eruption. *J. Volcanol. Geotherm. Res.* **2000**, *95*, 309–317. https://doi.org/10.1016/S0377-0273(99)00121-3
94. Sheridan, M.F.; Wohletz, K.H. Hydrovolcanism—Basic considerations and review. *J. Volcanol. Geotherm. Res.* **1983**, *17*, 1–29. https://doi.org/10.1016/0377-0273(83)90060-4
95. Morrissey, M.M.; Zimanowski, B.; Wohletz, K.; Büttner, R. Phreatomagmatic fragmentation. In *Encyclopedia of Volcanoes*, Sigurdsson, H., Houghton, B.F., McNutt, S.R., Rymer, H., Stix, J., Eds.; Academic Press: New York, NY, USA, 2000; pp. 431–446.
96. White, J.D.L.; Valentine, G.A. Magmatic versus phreatomagmatic fragmentation: Absence of evidence is not evidence of absence. *Geosphere* **2016**, *12*, 1478–1488. https://doi.org/10.1130/ges01337.1.
97. Németh, K.; Kosik, S. Review of Explosive Hydrovolcanism. *Geosciences* **2020**, *10*, 44. https://doi.org/10.3390/geosciences10020044.
98. Buchanan, D.J.; Dullforce, T.A. Mechanism for Vapour Explosions. *Nature* **1973**, *245*, 32–34. https://doi.org/10.1038/245032a0.
99. Lorenz, V. On the growth of maars and diatremes and its relevance to the formation of tuff rings. *Bull. Volcanol.* **1986**, *48*, 265–274. https://doi.org/10.1007/BF01081755
100. Buttner, R.; Dellino, P.; La Volpe, L.; Lorenz, V.; Zimanowski, B. Thermohydraulic explosions in phreatomagmatic eruptions as evidenced by the comparison between pyroclasts and products from Molten Fuel Coolant Interaction experiments. *J. Geophys. Res. -Solid Earth* **2002**, *107*, art. no.-2277. https://doi.org/10.1029/2001JB000511
101. Head III, J.W.; Wilson, L. Lava fountain heights at Pu'u 'O'o, Kilauea, Hawaii: Indicators of amount and variations of exsolved magma volatiles. *J. Geophys. Res. Solid Earth* **1987**, *92*, 13715–13719. https://doi.org/10.1029/JB092iB13p13715.
102. Head, J.W.; Wilson, L. Basaltic pyroclastic eruptions: Influence of gas release patterns and volume fluxes on fountain structure, and the formation of cinder cones, spatter cones, rootless flows, lava ponds and lava flows. *J. Volcanol. Geotherm. Res.* **1989**, *37*, 261–271. https://doi.org/10.1016/0377-0273(89)90083-8
103. Duraiswami, R.A.; Gadpallu, P.; Shaikh, T.N.; Cardin, N. Pahoehoe–a'a transitions in the lava flow fields of the western Deccan Traps, India-implications for emplacement dynamics, flood basalt architecture and volcanic stratigraphy. *J. Asian Earth Sci.* **2014**, *84*, 146–166. https://doi.org/10.1016/j.jseaes.2013.08.025.
104. Kilburn, C.R.J. Pahoehoe and aa lavas: A discussion and continuation of the model of Peterson and Tilling. *J. Volcanol. Geotherm. Res.* **1981**, *11*, 373–382. https://doi.org/10.1016/0377-0273(81)90033-0.
105. Walker, G.P.L. Volcanic rift zones and their intrusion swarms. *J. Volcanol. Geotherm. Res.* **1999**, *94*, 21–34. https://doi.org/10.1016/s0377-0273(99)00096-7.
106. Peterson, D.W.; Tilling, R.I. Transition of basaltic lava from pahoehoe to aa, Kilauea Volcano, Hawaii: Field observations and key factors. *J. Volcanol. Geotherm. Res.* **1980**, *7*, 271–293. https://doi.org/10.1016/0377-0273(80)90033-5.
107. Detay, M.; Hróarsson, B. Mise en place des pāhoehoe par tubes et tunnels de lave: Concept et signatures volcano-géomorphologiques. *Géomorphologie Relief Process Environ.* **2018**, *24*, 365–388. https://doi.org/10.4000/geomorphologie.12557
108. Kauahikaua, J.P.; Sherrod, D.R.; Cashman, K.V. Hawaiian lava-flow dynamics during the Pu'u O'o-Kupainaha eruption: A tale of two decades. In *The Pu'u O'o-Kupaianaha Eruption of Kilauea Volcano, Hawai'i: The first 20 years.*; Heliker, C., Swanson, D.A., Takahashi, T.J., Eds.; US Geological Survey, Boulder, Colorado USA: 2003; Volume US Geological Survey, Professional Paper 1676, pp. 63–88. https://doi.org/10.3133/pp167
109. Valentine, G.A. Shallow plumbing systems for small-volume basaltic volcanoes, 2: Evidence from crustal xenoliths at scoria cones and maars. *J. Volcanol. Geotherm. Res.* **2012**, *223*, 47–63. https://doi.org/10.1016/j.jvolgeores.2012.01.012.
110. Valentine, G.A.; White, J.D.L. Revised conceptual model for maar-diatremes; subsurface processes, energetics, and eruptive products. *Geology* **2012**, *40*, 1111–1114. http://dx.doi.org/10.1130/G33411.1.
111. Lorenz, V. Maar-diatreme volcanoes, their formation, and their setting in hard-rock or soft-rock environments. *Geolines J. Geol. Inst. AS Czech Repub.* **2003**, *15*, 72–83.

112. Auer, A.; Martin, U.; Németh, K. The Fekete-hegy (Balaton Highland Hungary) "soft-substrate" and "hard-substrate" maar volcanoes in an aligned volcanic complex—Implications for vent geometry, subsurface stratigraphy and the palaeoenvironmental setting. *J. Volcanol. Geotherm. Res.* **2007**, *159*, 225–245. https://doi.org/10.1016/j.jvolgeores.2006.06.008.
113. White, J.D.L. Impure coolants and interaction dynamics of phreatomagmatic eruptions. *J. Volcanol. Geotherm. Res.* **1996**, *65*, 155–170. https://doi.org/10.1016/S0377-0273(96)00061-3
114. Németh, K.; Martin, U.; Harangi, S. Miocene phreatomagmatic volcanism at Tihany (Pannonian Basin, Hungary). *J. Volcanol. Geotherm. Res.* **2001**, *111*, 111–135. https://doi.org/10.1016/s0377-0273(01)00223-2.
115. Kervyn, M.; Ernst, G.G.J.; Carracedo, J.C.; Jacobs, P. Geomorphometric variability of "monogenetic" volcanic cones: Evidence from Mauna Kea, Lanzarote and experimental cones. *Geomorphology* **2012**, *136*, 59–75. https://doi.org/10.1016/j.geomorph.2011.04.009.
116. Wood, C.A. Morphometric evolution of cinder cones. *J. Volcanol. Geotherm. Res.* **1980**, *7*, 387–413. https://doi.org/10.1016/0377-0273(80)90040-2
117. Lamb, H.F.; Damblon, F.; Maxted, R.W. Human Impact on the Vegetation of the Middle Atlas, Morocco, During the Last 5000 Years. *J. Biogeogr.* **1991**, *18*, 519–532. https://doi.org/10.2307/2845688.
118. Nahid, A. Le Quaternaire Continental Marocain. Tome 1: Six Décennies d'évolution Des Idées Sur Les Méthodes et Concepts En Chronostratigraphie Du Quaternaire Continental Marocain: Entre Les Difficultés Incertitudes Progrès **2001**. 1-179, Marrakech, Morocco, ISBN: 322-2001 IFBN9954-0-0792-X
119. Lenhardt, N.; Borah, S.B.; Lenhardt, S.Z.; Bumby, A.J.; Ibinoof, M.A.; Salih, S.A. The monogenetic Bayuda Volcanic Field, Sudan—New insights into geology and volcanic morphology. *J. Volcanol. Geotherm. Res.* **2018**, *356*, 211–224. https://doi.org/10.1016/j.jvolgeores.2018.03.010.
120. van Wyk de Vries, B.; Matela, R. Styles of volcano-induced deformation: Numerical models of substratum flexure, spreading and extrusion. *J. Volcanol. Geotherm. Res.* **1998**, *81*, 1–18.
121. Acocella, V.; Neri, M. Dike propagation in volcanic edifices: Overview and possible developments. *Tectonophysics* **2009**, *471*, 67–77. https://doi.org/10.1016/j.tecto.2008.10.002.
122. Carn, S.A. The Lamongan volcanic field, East Java, Indonesia: Physical volcanology, historic activity and hazards. *J. Volcanol. Geotherm. Res.* **2000**, *95*, 81–108. https://doi.org/10.1016/S0377-0273(99)00114-6
123. Lutz, T.; Gutmann, J. An improved method for determining and characterizing alignments of pointlike features and its implications for the Pinacate volcanic field, Sonora, Mexico. *J. Geophys. Res. Solid Earth* **1995**, *100*, 17659-17670. https://doi.org/10.1029/95jb01058.
124. Le Corvec, N.; Spoerli, K.B.; Rowland, J.; Lindsay, J. Spatial distribution and alignments of volcanic centers: Clues to the formation of monogenetic volcanic fields. *Earth Sci. Rev.* **2013**, *124*, 96–114. https://doi.org/10.1016/j.earscirev.2013.05.005.
125. Ort, M.H.; Carrasco-Nunez, G. Lateral vent migration during phreatomagmatic and magmatic eruptions at Tecuitlapa Maar, east-central Mexico. *J. Volcanol. Geotherm. Res.* **2009**, *181*, 67–77. https://doi.org/10.1016/j.jvolgeores.2009.01.003.
126. Cas, R.; Wright, J. *Volcanic successions, modern and ancient*; Allen and Unwin: London, UK, 1987; p. 528. http://dx.doi.org/10.1007/978-94-009-3167-1
127. Sato, H. Textural Difference between Pahoehoe and Aa Lavas of Izu-Oshima Volcano, Japan—An Experimental-Study on Population-Density of Plagioclase. *J. Volcanol. Geotherm. Res.* **1995**, *66*, 101–113. https://doi.org/10.1016/0377-0273(94)00055-L
128. Polacci, M.; Corsaro, R.A.; Andronico, D. Coupled textural and compositional characterization of basaltic scoria: Insights into the transition from Strombolian to fire fountain activity at Mount Etna, Italy. *Geology* **2006**, *34*, 201–204. https://doi.org/10.1130/g22318.1.
129. Murcia, H.; Németh, K.; Lindsay, J.; Moufti, M.R.; El-Masry, N.; Cronin, S.J.; Smith, I.E.M. Complex isolated-to-nested pyroclastic cones and cone rafting in the AD 1256 Al-Madinah fissure eruption in the Kingdom of Saudi Arabia. In: Buechner J, Rapprich V, Tietz O. (Eds) Abstract Book & Excursion Guides - Basalt 2013 - *Cenozoic Magmatism in Central Europe*, Goerlitz, Germany, 24 Apr 2013 - 28 Apr 2013, **2013**, 174–175.
130. Sumner, J.M. Formation of clastogenic lava flows during fissure eruption and scoria cone collapse: The 1986 eruption of Izu-Oshima Volcano, eastern Japan. *Bull. Volcanol.* **1998**, *60*, 195–212. https://doi.org/10.1007/s004450050227.
131. Maro, G.; Caffe, P.J. Neogene monogenetic volcanism from the northern Puna region; products and eruptive styles. *Spec. Publ. Geol. Soc. Lond.* **2016**, *446*, 337–359, 323. http://dx.doi.org/10.1144/SP446.6.